J. Magn. Soc. Jpn., 36, 268-271 (2012)

Decreasing Coupling between Feeding Coils for Functional Electrical Stimulation with Direct Feeding Method

K. Kato, K. Iwasaki, K. Furiya, N. Tamura*, T. Satoh, T. Takura*, F. Sato*, H. Matsuki
Graduate School of Bmd. Eng., Tohoku Univ., *6-6-05 Aoba Aramaki-aza, Aoba-ku, Sendai 980-8579, Japan*
*Graduate School of Eng., Tohoku Univ., *6-6-05 Aoba Aramaki-aza, Aoba-ku, Sendai 980-8579, Japan*

Functional electrical stimulation (FES) is a therapy used to rehabilitate patients with lost movement functions, and to apply stimulations. We adapted a method of implanted direct feeding method to apply stimulation as part of this therapy. Stimulus energy and signals for controlling devices are applied to devices by utilizing a mounted system using magnetic coupling. Power feeding is presently carried out with a serial resonance circuit in the method of direct feeding. Two feeding coils are used for the upper and lower arms individually in order not to disturb the movement in the joint of the elbow. Declination of resonance from variations in coupling interference from the movement of feeding coils is a problem. To solve it, we used a method that reduced variations in coupling interference by using a short coil between feeding coils. We report here the result of experiments conducted on this method.

Key words: Functional electrical stimulation, direct feeding method, implant stimulator

直接給電 FES 用体外励磁装置間の結合干渉の低減方式

加藤健太郎・岩崎圭祐・降矢健太郎・田村直樹*・佐藤忠邦・田倉哲也*・佐藤文博*・松木英敏
東北大学大学院医工学研究科，仙台市青葉区荒巻字青葉 6-6-05（〒980-8579）
*東北大学大学院工学研究科，仙台市青葉区荒巻字青葉 6-6-05（〒980-8579）

1. はじめに

1.1. FES について

脳卒中や脊髄損傷などにより四肢麻痺が生じたとしても，筋肉が興奮性を保持している場合がある．この場合，筋に電気刺激を印加することによって筋収縮を誘発することができる．この現象を利用して失われた運動機能を再建しようとする治療法を機能的電気刺激（FES：functional electrical stimulation）という[1-3]．この FES を実現するに当たり，我々は直接給電法によるインプラント刺激素子（implant stimulator）の実現を目指してきた[4]．

1.2. 直接給電法について

直接給電法では，インプラント刺激素子を刺激箇所近傍に埋め込み刺激を行うため，局所刺激が可能となり，無痛・低疲労・低消費電力な刺激が可能となる．また，このインプラント刺激素子へは，体外装着コイル（mounted coil）とインプラント刺激素子に実装されているインプラントコイルを用いた電磁誘導による非接触エネルギー伝送と体内外間における双方向通信を行う（Fig. 1）．そのため，体外装着コイルおよびインプラントコイルは，給電コイル（feeding coil）および通信コイル（communication coil）から構成されている．本検討では，体外から体内へのエネルギー伝送にのみ着目している．将来的には本システムの全身への適用を目指しているが，その初段階として本研究では上肢への適用に限定して検討を行っている．上腕全体に埋め込まれたインプラント刺激素子への給電・通信を可能にするために，体外装着コイルは上腕を広く覆うような形状をとる必要がある．体内の受電および通信コイルは，体外装着コイルとの結合を補うため棒状フェライトコアを用いて実現されており，小型化の観点から各コイルは同一のコア上に実現されている．

1.3. 体外励磁システムの問題点

実際に体外励磁コイルを用いて給電を行う際には，日常生活に用いることを考えシステムはポータブルなものが求められる．このため，体外装置の電源として電池を用いることを想定している．電池を用いて給電に必要とされるコイル端電圧を得るためには直列共振によるインピーダンスの低減が不可欠となる．電源と体外励磁コイルの間に直列にコンデンサを挿入することで共振を取り，電源への負担を低減している．しかし，コンデンサを用いて給電を行う際の問題点がある．上肢全体に埋め込まれたインプラント刺激素子への給電を行うにあたり肘関節の動きを妨げないようにするため，上腕と前腕にそれぞれ体外励磁コイルが必要となる．

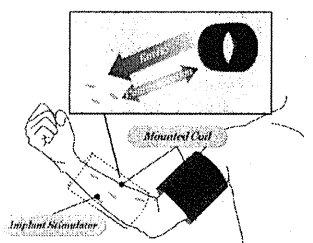

Fig. 1 Direct feeding FES system.

しかし，前腕と上腕に給電コイルを用いた場合，給電コイル間での結合が生じる．その結合は肘関節の動きにより，上肢の伸展・屈曲が生じることで変化が生じる．肘関節の動きによる体外励磁コイル位置の変化を Fig. 2 に示す．この変化によって，共振が取れなくなり安定した給電が出来なくなってしまう．体外励磁コイルの一次側から見たインピーダンスの式を下の式(1)に示す．

$$Z_{in} = r_p\left[1+\frac{k_p^2}{\frac{1}{Q_p^2}+1}+jQ_p\left(1-\frac{k_p^2}{\frac{1}{Q_p^2}+1}\right)\right] \quad \cdots(1)$$

r_p, L_p, Q_pはそれぞれ体外励磁コイルの抵抗，インダクタンス，Q 値となっている．k_pは体外励磁コイル間の結合係数である．この式のインダクタンスの項に着目する．k_pの変化が大きいとインダクタンスの変化が大きくなり，共振が狂れてしまう．

実際に給電コイル同士の位置を変化させて給電を行った時のインプラントコイルで得られる受電電力の変化とそのときの結合係数 k_pの関係を Fig. 3 に示す．k_pの変化範囲における平均値を示すθ= 20 degree において共振を取り，このときの受電電力を用いて規格化している．Fig. 3 より，共振がとれている点においては十分な電力が受電可能であるが，共振を取っている点から位置が変化していくことで著しく受電電力が小さくなっていることがわかる．関節可動域はθ= 0 から 145 degree であり，本設計のままでは実仕様に適さない．また，θ= 180 degree においては k_pがθ= 20 degree とほぼ一致していることから，高い受電電力が得られる．このことから，受電電力の変化は共振を設計した際の結合係数からの差分に依存するものであることがわかる．

この問題に対して，先行研究において時分割駆動を用いた方式が解決策として挙げられていた[2]．この方式では，体内刺激素子で受電，整流後に波形を平滑する平滑コンデンサが体内素子に対して大きすぎるため体内素子に用いるにあたって問題となる．

これを解決するため，本検討ではショートコイルを用いた体外励磁コイル間の結合低減方式を提案したので，これについて報告する．

2. 給電コイル間の結合干渉低減方式

2.1 結合干渉低減方式の原理

体外励磁コイル間の結合係数において結合変動が大きい部分での結合変動の低減を目的とする．そのため今回はショートコイルを用いた検討を行った．ショートコイルを体外励磁コイルの磁束が鎖交する範囲に配置することで打ち消す磁束を発生させる．体外励磁コイルから発生した磁束がショートコイルを貫くことによって，ショートコイルに磁束を打ち消す向きに誘導電流が流れる．ショートコイルからの磁束により体外励磁コイルからの磁束をシールドすることになる．給電コイルからの磁束がショートコイルによりシールドされている図を Fig. 4 に示す．Fig. 4 は磁束分布を示している．図の中央に体外励磁コイルを配置し，体外励磁コイルの上部に隣接させる形でショートコイルを配置している．色の薄い部分が磁束密度の高い範囲，色の濃い部分が磁束密度の低い範囲となっている．体外励磁コイルのみである下部のコイル端 B と比べてショートコイルを配置した上部のコイル端 A でθ = 0 degree 方向の磁束密度がよく打ち消されていることがわかる．

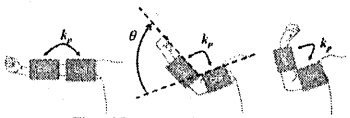

Fig. 2 Movement of feeding coils by motion of joint in elbow.

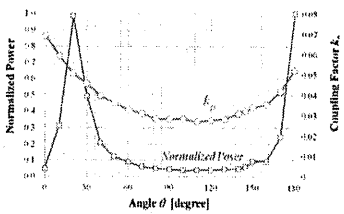

Fig. 3 Normalized power and coupling factor with angle of feeding coils.

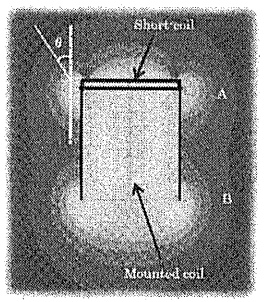

Fig. 4 Magnetic flux distribution with short coil.

2.2 結合干渉測定方法

2 つの体外励磁コイルに対し，2 つのショートコイルを用いた．測定を行うシステムを Fig. 5 に示す．体外励磁コイルのパラメータは上腕に装着可能な直径 90 mm，全長 110 mm，巻数 50 turns のソレノイドコイルである．ショートコイルは直径 90 mm，巻数 4 turns のソレノイドコイルである．磁束が鎖交する範囲にショートコイルを配置するため，ショートコイルはそれぞれの体外励磁コイルに隣接した．また，システムが対称形を取るようにするため，2 つの体外励磁コイルの間に配置されるようにした．この状態

で，関節の可動域を想定して角度を変化させたときの体外励磁コイル間の結合干渉を測定した．2つの体外励磁コイルと2つのショートコイルが一直線に並んだ状態を$\theta = 0$ degreeとして$\theta = 180$ degreeまで角度を変化させたときの結合度として式(2)を定義した．

$$k' = \sqrt{1 - \frac{L_{short}}{L_{open}}} \qquad \cdots(2)$$

ショートコイルを体外励磁コイルの間に配置したときの，体外励磁コイル間の見かけ上の結合を「結合干渉」と定義する．k'は結合干渉の値である．L_{open}は二次側の体外励磁コイルを開放した場合の自己インダクタンス値．L_{short}は二次側の体外励磁コイルを短絡した場合の自己インダクタンス値である．一次側と二次側の体外励磁コイルの結合干渉の値を調べるので，ショートコイルは常に短絡の状態とした．

2.3 結合干渉測定結果

結合干渉の測定を行った結果をFig. 6に示す．縦軸が結合干渉の値，横軸がθとなっている．Fig. 6より，原理で示した通りに$\theta = 0$ degreeにおいて結合干渉が0.07から0.02と著しく減少していることがわかる．$\theta = 0$ degreeにおいて最も結合干渉の値が減少し，そこから角度が大きくなるにしたがってショートコイルがない場合からの減少量は小さくなっている．問題となっていた結合干渉の変化幅に着目してみると，関節可動域においてショートコイルがない場合は約0.04であることに対し，ショートコイルを配置した場合では約0.01と大きく減少した．ショートコイルを配置することで結合干渉の低減に有効であることが確認された．

2.4 考察

$\theta = 0$ degreeにおいて大幅に結合干渉が低減されたことから，原理で示した通り，ショートコイルによって体外励磁コイルから発生した磁束がシールドされたものと考えられる．$\theta = 0$ degreeにおいて大きく結合干渉が低減されたことで，ショートコイルがない場合に見られていた$\theta = 0$から90 degreeまでの急激な結合干渉が見られなくなった．$\theta = 180$ degreeに近づくにつれて結合干渉の値が増加しているが，関節可動域が$\theta = 0$から145 degreeとなっているためこの増加は問題ないと考えられる．これらのことより，角度が変化しても関節可動域において緩やかな結合干渉の変化となったと考えられる．また，結合干渉の変化量が減少したことからこれは実際の給電においても効果が期待できる．

3. 給電試験

3.1 実験方法

給電試験を行う際の構成として，コイルパラメータは2.2節と同一のものを用いた．実験系をFig. 7に示す．一次側の体外励磁コイルに電源を接続した．さらにコンデンサを用いて直列共振とした状態で励磁を行った．共振はFig. 6から関節可動域における結合干渉の中央値を示す$\theta = 0$ degreeで設計した．二次側の体外励磁装置はコンデンサを用いて直列共振とした状態で短絡した．体内側の刺激素子は一次側の体外励磁コイル(電源接続側)の中央部分に配置して受電を行った．刺激素子は0.7 mm×0.7 mm×10 mmの角柱フェライトに銅線を巻きつけたものを用いた．周波数は100 kHzとした．体内素子側に1 kΩの負荷を用いて受電を行った．体外励磁コイル同士の位置が変化したときの一次側の体外励磁コイル内に設置された刺激素子の受電電力を測定した．

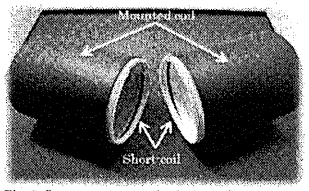

Fig. 5 System using method of coupling lowering.

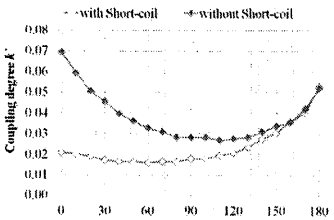

Fig. 6 Coupling interference with short coil.

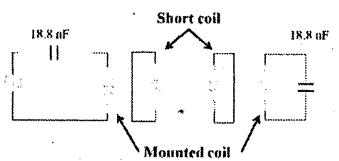

Fig. 7 Experimental system.

3.2 実験結果

給電試験を行った結果のグラフをFig. 8に示す．縦軸は刺激素子における受電電力を最大値で規格化した値となっている．横軸は体外励磁コイル同士の角度θである．Fig. 3よりショートコイルを配置しない場合は共振点以外で全く刺激素子での受電が出来ていないかったが，Fig. 8よりショートコイルを配置した場合は関節可動域である$\theta = 0$から145 degreeにおいてすべての範囲で大きな電力が受電出来ている．このことより関節の可動域において，ショートコイルを配置した場合の方が安定した給電が可能となっていることが分かる．

3.3 考察

Fig. 8より，受電電力は$\theta = 60$ degree付近を中心に対称な形となっている．これはFig. 6におけるショートコイルを付けた場合の結合干渉に依存する．$\theta = 0$ degreeにおけるk'との差分を表したグラフをFig. 9に示す．Fig. 8と比較すると設計された条件からk'が離れるほど受電電力が小さくなっていることがわかる．$\theta = 0$ degreeにおけるk'の値はθが大きくなるにつれて徐々にずれていくが，$\theta = 120$ degree付近で再びk'が一致したことにより受電電力を大きくする結果となったことが分かる．このことは，k'の角度依存性を小さくすることが安定した受電につながることを示唆している．

ショートコイルを配置することにより関節可動域においてすべての範囲で受電電力を大きくすることが出来た．しかし，結合干渉の値の変化がほとんどないにも関わらず受電電力は大きく変化した．このことについて検討するため，1.3節の式(1)の虚部の項に着目する．結合干渉の変化が小さいとしても，Q値が高い場合にインピーダンスの虚部項の変化が大きくなる．そのために共振条件が崩れ，受電電力が減少していると考えられる．

4. まとめと今後の課題

今回の検討より，ショートコイルを体外励磁コイルに隣接させることで磁束がシールドされ，結合が低減されることが確認された．このことから，この結合低減方式の効果が確認された．また，結合低減方式を用いての給電試験を行うことで刺激素子における受電電力の安定化も確認された．

今後，この方式を利用していくに当たって課題となるのが，さらなる受電電力の安定化である．今回の検討で受電電力の変動が大幅に改善された．しかし理想としては変動が0となることが求められる．よって今後今回の方式を応用してさらなる受電電力の安定化を目指す．

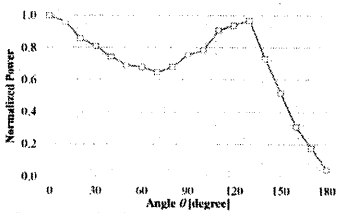

Fig. 8 Normalized receiving power with short coil.

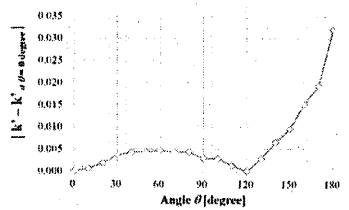

Fig. 9 Difference of k' from resonance condition.

References

1) N. Hoshimiya: *Journal of Japanese Society for Medical and Biological Engineering*, Vol. 6, 8, 1-7(1992)
2) Y. Handa: *Journal of Society of Biomechanisms Japan*, Vol. 17 , 1,(1993)
3) Y. Shimada and M. Ichie: *Journal of the Society of Instrument and Control Engineers*, Vol. 33, 4, 321 - 326, (1994)
4) F. Sato, T. Nomoto, H. Matsuki and T. Satoh: *IEEE Trans. Magn.*, 40, 2964-2966,2004
5) Y. Kohata, K. Kato, T. Sato, T. Takura, F. Sato, H. Matsuki, K. Seki and Y. Handa : Tohoku-Section Joint Convention Record of Institutes of Electrical and Information Engineers, Japan, 230 (2009)

2011年 10月 28日受理，2012年 2月 10日採録

Computer Methods in Biomechanics and Biomedical Engineering
Vol. 15, No. 7, July 2012, 771–778

Taylor & Francis
Taylor & Francis Group

Patient-specific modelling of pulmonary airflow using GPU cluster for the application in medical practice

T. Miki[a]*, X. Wang[b], T. Aoki[b], Y. Imai[c], T. Ishikawa[c], K. Takase[d] and T. Yamaguchi[a]

[a]*Department of Biomedical Engineering, Tohoku University, Aoba 6-6-01, Sendai 980-8579, Japan;* [b]*Global Scientific Information and Computing Center, Tokyo Institute of Technology, O-okayama 2-12-1, Meguro-ku, Tokyo 152-8550, Japan;* [c]*Department of Bioengineering and Robotics, Tohoku University, Aoba 6-6-01, Sendai 980-8579, Japan;* [d]*Department of Diagnostic Radiology, Tohoku University, Seiryo-machi 1-1, Sendai 980-8574, Japan*

(*Received 25 October 2010; final version received 3 February 2011*)

In this paper, we propose a novel patient-specific method of modelling pulmonary airflow using graphics processing unit (GPU) computation that can be applied in medical practice. To overcome the barriers imposed by computation speed, installation price and footprint to the application of computational fluid dynamics, we focused on GPU computation and the lattice Boltzmann method (LBM). The GPU computation and LBM are compatible due to the characteristics of the GPU. As the optimisation of data access is essential for the performance of the GPU computation, we developed an adaptive meshing method, in which an airway model is covered by isotropic subdomains consisting of a uniform Cartesian mesh. We found that 4^3 size subdomains gave the best performance. The code was also tested on a small GPU cluster to confirm its performance and applicability, as the price and footprint are reasonable for medical applications.

Keywords: pulmonary airflow simulation; patient-specific modelling; high-performance computing; multi-GPU computation; lattice Boltzmann method

1. Introduction

Computational fluid dynamics (CFD) studies on pulmonary airflow started in the early 1990s (Balásházy and Hofmann 1993a, 1993b) and have contributed to revealing respiratory mechanics using ideal airway models (Nowak et al. 2003; Zhang et al. 2005; Yang et al. 2006). To understand the mechanics in more detail and for practical studies, patient-specific models constructed from medical images have been used in the twenty-first century. van Ertbruggen et al. (2005) computed the deposition of inhaled microparticles using a realistic airway model, while De Backer et al. (2008) measured the change in airflow resistance in the lungs of patients with asthma before and after bronchodilator administration. Modern computational techniques most often used in pulmonary airflow simulations are the finite volume method (Gemci et al. 2008) and finite element method (Lin et al. 2007), which are computed on airway models consisting of tetrahedral elements. Recently, De Backer et al. (2010) compared numerical results with *in vivo* measurement data and reported on the validity of numerical pulmonary airflow simulation. As the pulmonary airway tree has many peripheral airways in which outlet boundary conditions should be given, several researchers (Comeford et al. 2010; Yin et al. 2010) have studied the estimation of outlet boundary conditions for each outlet. Based on these studies, patient-specific CFD computation will soon be applied to the diagnosis and treatment of respiratory diseases such as asthma and bronchiectasis. As disease symptoms arise from unusual airflow behaviour, identifying precise airflow features in each patient is important, while geometric analysis and spirometry are currently used in respiratory diagnosis. CFD can predict the effects of local airway obstruction and dilation on overall respiratory function, or it can be applied to custom-made drug-delivery systems. The visualisation of airflow will also help both medical doctors and patients understand what is occurring in a patient's body.

Nevertheless, computational time is a barrier to achieving the practical use of such methods. The pulmonary airways are multi-level bifurcating passages that require a huge computational mesh to resolve the flow field in all bronchi, and rapid simulation is crucial to the clinical application of patient-specific modelling. One possible approach is parallel computing, and parallel CFD on a central processing unit (CPU) cluster is now commonly used in commercial software. Parallel CFD using a cluster system with a massive number of CPUs, such as the machines on the Top500 list of supercomputers, may overcome the problem, but few people can access such resources. This is particularly important when we consider the use of computing in medicine, as most clinicians can only afford low cost, small-footprint computer systems. Recently, parallel CFD on graphics processing units (GPUs) has attracted interest as a new innovation in CFD simulation. A GPU contains hundreds of streaming processors and is attached to very wide-bandwidth device memories. Because nVIDIA introduced the general-purpose GPU computing library, the Compute Unified Device Architecture (CUDA) in 2006, many researchers have attempted GPU computation for a variety of CFD problems (Corrigan et al. 2010; Thibault and Senocak 2010).

In this paper, we propose a novel patient-specific method of modelling pulmonary airflow using multi-GPU computation. Conventional patient-specific models use semi-implicit methods to solve incompressible flow, but most of the computational time is consumed in the iterative procedure used to solve the pressure Poisson equation due to very slow convergence. Instead, we use the lattice Boltzmann method (LBM), a fully explicit incompressible flow solver. The simple vectorised operations of the LBM are suitable for GPU computation. In addition, the performance of the LBM strongly depends on memory bandwidth, due to many variables included in the computation; hence, the LBM can benefit from GPU computation. Some studies (Zhao 2008; Riegel et al. 2009; Kuznik et al. 2010; Tölke 2010) have reported the capacity of GPU computation with the LBM (GPU-LBM).

However, the computational mesh must be well designed for GPU-LBM computation, as coalesced memory access and reduced access to GPU device memory are essential in the CUDA programming model. Here, we apply a Cartesian mesh, which is suitable for both memory access and patient-specific modelling. As medical image data consist of voxels aligned using Cartesian co-ordinates, a Cartesian mesh can be generated directly from the data, whereas a tetrahedral mesh, often used in conventional patient-specific modelling, requires laborious mesh generation. When we use a Cartesian mesh consisting of cuboid domains, the data are inherently structured, which is adequate for GPU computation. However, such a simple cuboid domain results in much unnecessary mesh because the pulmonary airway is a set of long branches and occupies a very small region in medical image data. Conversely, if we eliminate the unnecessary mesh, the data become unstructured. In this case, each mesh component must know the dependency of the neighbouring mesh components, and the data position of each mesh component is independent of its geometric position, bringing in non-coalesced memory access and many accesses to the device memory. Hence, GPU-LBM computation has not been developed for complex geometry problems. To overcome this drawback, we developed an optimal meshing method that retains the features of both structured and unstructured meshes.

*Corresponding author. Email: takahito@pfsl.mech.tohoku.ac.jp

ISSN 1025-5842 print/ISSN 1476-8259 online

http://dx.doi.org/10.1080/10255842.2011.560842
http://www.tandfonline.com

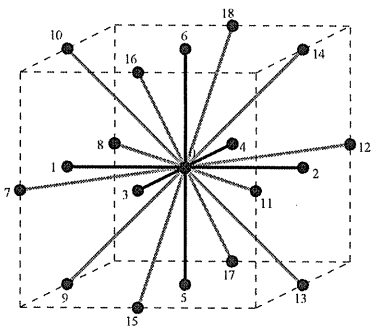

Figure 1. The D3Q19 lattice model.

2. Lattice Boltzmann method

The LBM is a numerical scheme for flow simulation based on the application of the Boltzmann equation to the analysis of molecular movement. In the LBM, a continuous fluid is represented by ideal particles, which move only along a restricted path (the lattice) at a limited speed. In this study, we apply the D3Q19 lattice model as shown in Figure 1 for an isothermal incompressible airflow.

The movement of the particles is simply expressed by collision and streaming steps described in the lattice Boltzmann equation:

$$f_i(x + c\Delta t, t + \Delta t) = f_i(x, t) + \Omega[f_i(x, t)], \qquad (1)$$

where f_i is the particle distribution heading in direction $i = 0$–18, and Δt is the time interval. As the distance which the particles travel is limited to adjacent lattice points at every time step, the particle speed c can only take the values

$$c = \begin{cases} 0, & \text{for } i = 0 \\ \Delta x/\Delta t, & \text{for } i = 1 \sim 6 \\ \sqrt{2}\Delta x/\Delta t, & \text{for } i = 7 \sim 18 \end{cases}, \qquad (2)$$

where Δx is the lattice spacing and Ω is the collision operator for which the lattice Boltzmann–Gross–Krook (LBGK) model (Qian et al. 1992) is often applied. The LBGK equation is

$$f_i(x + c\Delta t, t + \Delta t) = f_i(x, t) + \frac{1}{\tau}\left\{f_i^{\mathrm{eq}}(x, t) - f_i(x, t)\right\}, \qquad (3)$$

$$f_i^{\mathrm{eq}} = t_p\rho\left[1 + \frac{c_{i\alpha}u_\alpha}{c_s^2} + \frac{u_\alpha u_\beta}{2c_s^2}\left\{\frac{c_{i\alpha}c_{i\beta}}{c_s^2} - \delta_{\alpha\beta}\right\}\right], \qquad (4)$$

where the subscripts α and β represent a direction in Cartesian co-ordinates, δ is the Kronecker delta and t_p is a coefficient that depends on the particle direction, i.e. $t_0 = 1/3$ for $i = 0$, $t_1 = 1/18$ for $i = 1-6$ and $t_2 = 1/36$ for $i = 7-18$. The LBGK equation satisfies the equation of continuity and the Navier–Stokes equation. τ is the relaxation time: the amount of time until the local particle distribution reaches equilibrium after particle collisions represented by

$$\tau = \frac{\nu}{c_s^2} + \frac{1}{2}, \tag{5}$$

using the fluid kinetic viscosity ν. c_s is the speed of sound, related to the particle speed in the LBGK model by

$$c_s = \frac{1}{\sqrt{3}} c. \tag{6}$$

The macroscopic fluid variables density ρ, velocity u_α and pressure P can be obtained from the following equations:

$$\rho = \sum_{i=0}^{18} f_i, \tag{7}$$

$$\rho u_\alpha = \sum_{i=0}^{18} f_i c_{i\alpha}, \tag{8}$$

$$P = c_s^2 \rho, \tag{9}$$

using the microscopic variable f_i. As shown above, the solution procedure is fully explicit, and no iterative solver is necessary in the LBM.

The GPU code was developed with CUDA version 3.1 (CUDA C programming guide 2010) and all of the macroscopic and microscopic fluid variables were computed in single precision. The bounce-back condition was applied to satisfy the no-slip condition at the airway wall. The tracheal inlet boundary condition is described by a prescribed flow velocity. The computations performed in this study are all computed with a tracheal Reynolds number in 1500 with a parabolic velocity profile; hence, laminar flow can be assumed in most of the computational domain. The outlet boundary condition to the outermost peripheral airways is given by a fixed pressure. As the pulmonary airways have a branched geometry, the boundary condition should be estimated for each outermost airway to obtain a better solution (Comeford et al. 2010; Yin et al. 2010). However, in this paper, we mainly discuss the applicability of the GPU-LBM to medical practice. For CFD simulation of any complex geometry, the code is implemented to compute the outlet and inlet boundary conditions facing arbitrary directions. Overall velocity distribution represented in this study qualitatively agreed with other pulmonary airflow studies (Rochefort et al. 2007; Freitas and Schröder 2008), for example, with respect to secondary vortexes, although the patient-specific airway models used in their study and our study are different.

3. Adaptive meshing method

For this study, a subject-specific voxel airway model was constructed from the computed tomography (CT) data of a 41-year-old male using in-house airway-lumen extraction software based on the region-growing method. We built a 13-generation airway model consisting of a fluid mesh with 7,746,378 cubes measuring 0.215^3 mm^3, as shown in Figure 2. The term 'generation' indicates the number of branches from the trachea to the outermost peripheral airways. As the CT data consist of voxels aligned in Cartesian co-ordinates, a computational mesh can easily be generated from the CT data using a Cartesian mesh.

According to the CUDA C best practices guide (2010), coalesced memory access and less access to GPU device memory are necessary to bring out the performance of the GPU computation. The term 'coalesced memory access', in GPU computation, indicates memory access to successive data blocks within a certain size at one time. This is achieved easily on the simple cuboid domains created with a Cartesian mesh. However, the use of a simple cuboid domain covering the entire airway model is uneconomical because the pulmonary airway is a set of long branches, which occupies a very small region in the CT data. Therefore, we propose an adaptive meshing

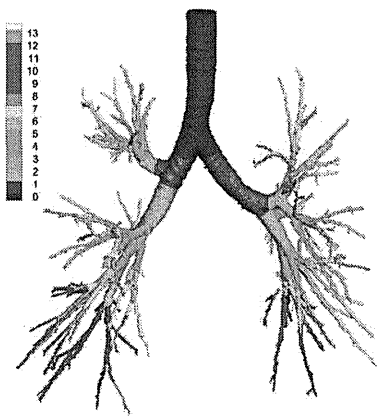

Figure 2. A 13-generation airway model: colour distribution indicates generation number of airways.

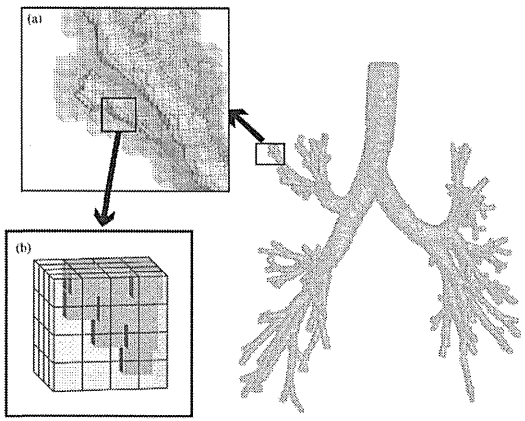

Figure 3. Schematic illustration of the adaptive meshing method: (a) the airway model is decomposed by isotropic subdomains and (b) each subdomain consists of a structured Cartesian mesh. As an example, a 4^3 size subdomain is drawn.

method: decomposing the airway into small isotropic subdomains consisting of a uniform Cartesian mesh, as shown in Figure 3. Each subdomain includes information on its connectivity to the neighbouring subdomains. Consequently, the global computational domain comprises unstructured subdomains, while the local subdomain consists of a structured Cartesian mesh, as shown in Figure 4. Although it may include unnecessary parts of the mesh in the computational domain, some recent LBM studies have used a similar form of domain decomposition (Stürmer et al. 2009; Palabos 2010) to adapt complex geometries to CPU parallel computation. In our study, decomposition is used to optimise memory access for the GPU computation. We compute each subdomain in a CUDA block, in which the block is a group of processes consisting of CUDA threads. Based on this, rather than one thread, several threads in a block co-operatively access each direction of the subdomain connectivity information at once via coalesced memory access, which accelerates the calculation.

Note that the size of the subdomains should be determined carefully because the ratio of the airway mesh to the entire mesh is highly dependent on this, and it also changes the appropriate number of CUDA threads for the computation in a subdomain. To determine the optimal subdomain size, we evaluated the filling ratio, two performance indices and memory usage. The filling ratio compares the number of airway (fluid) mesh components (N_a) to the total number of mesh components (N_g), including the unnecessary mesh components, and it is defined by

$$\text{Filling ratio} = \frac{N_a}{N_g}. \tag{10}$$

The two GFLOPS performance indices used are

$$\text{Real performance (GFLOPS)} = \frac{O \times N_g}{T \times S} \frac{1}{1024^3}, \tag{11}$$

$$\text{Effective performance (GFLOPS)} = \frac{O \times N_a}{T \times S} \frac{1}{1024^3}. \tag{12}$$

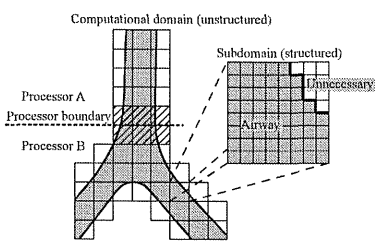

Figure 4. Schematic illustration of mesh hierarchy. The area in grey represents airway mesh, and the area in white is unnecessary mesh. Processor boundary in multi-GPU computation is also shown. Subdomains near processor boundary are indicated by the shaded area.

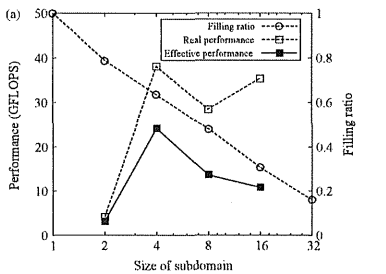

Figure 5. Results of the tests to determine the optimal subdomain size: (a) the filling ratio and performance indices and (b) memory usage.

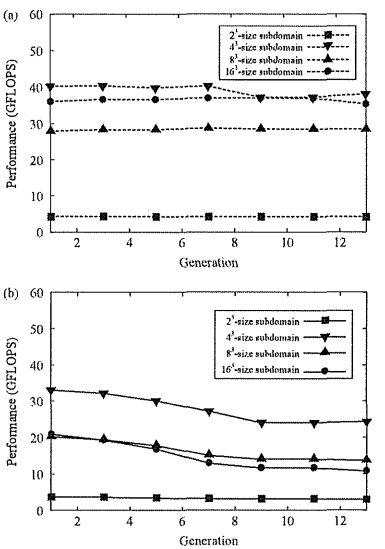

Figure 6. Effects of geometry complexity: (a) real performance and (b) effective performance.

In these, O is the number of floating-point operations ($O = 229$ in our D3Q19 LBGK model), T is the computational time and S is the number of computational steps. From the definition, the real performance represents the effort expended for the entire domain and the effective performance is the effort expended for the airway domain.

Figure 5(a) shows the results for the computation of the airway model in Figure 2 for subdomain sizes ranging from 1^3 to 32^3, performed on an nVIDIA Tesla C1060 GPU. As a large subdomain includes many unnecessary mesh components, the filling ratio decreases as the subdomain size increases. The real performance of a 2^3 size subdomain is the poorest, as only eight threads, which is smaller than the warp size, are used to compute one subdomain according to our CUDA block usage. The term 'warp' refers to the group of threads processed at one time; one warp consists of 32 threads for CUDA version 3.1, whereas 64 threads are used in a 4^3 size subdomain computation and 256 threads are used in 8^3 size and 16^3 size subdomain computations. The real performance of 4^3 size to 16^3 size subdomains ranges between 30 and 40 GFLOPS. However, the filling ratio decreases for the larger subdomains, and the effective performance is the highest for the 4^3 size subdomain. The memory usage for stored fluid variables and domain data is shown in Figure 5(b). As the subdomain size increases, the memory used to store fluid variables increases due to the increase in unnecessary mesh components. The subdomain connectivity information is stored for the entire mesh in the case of 1^3 size subdomains; thus, the memory usage for the domain data is the greatest. The minimum memory usage occurs using 4^3 size subdomains. To check whether the optimum subdomain size is affected by the complexity of geometry, we compared different geometries that were constructed by pruning airway branches from the original 13-generation airway model. We constructed 1- to 13-generation airway models, in which the complexity increases with the number of generations. The result is shown in Figure 6. The effective performance decreases as the geometry becomes more complex, owing to the decrease in the filling ratio, whereas the real performance is affected less by the geometry complexity for all subdomain sizes. In conclusion, GPU computations using 4^3 size subdomains have the greatest effective

performance for any airway model. An airway model covered by 4^3 size subdomains, consisting of 11,265,536 mesh components with 176,024 subdomains, is shown in Figure 3.

4. Comparison of the performance of multi-GPU and multi-CPU computations

We adapted the patient-specific model to multi-GPU computation using a message passing interface (MPI) library. As all of the fluid variables are stored in the GPU device memory and updated at every time step, additional data transfer protocols are needed compared with multi-CPU computation. First, the data in the device memory are transferred to the host computer memory through a PCI Express bus. After the data transfer, the data are exchanged among cluster nodes through InfiniBand using the MPI library. Finally, the exchanged data are copied from the host memory to the device memory through the PCI Express bus. As the GPU has the ability to compute much faster than the CPU and additional data transfer protocols are needed for GPU computation, the data transfers easily become bottlenecks in terms of the overall computational time. To reduce these bottlenecks, the subdomains near the processor boundary, as shown in Figure 4, are computed first, then the data transfers and computation of non-processor boundary subdomains are processed simultaneously. As the mesh components are clustered into subdomains, domain decomposition for multi-GPU computation is accomplished easily. For domain decomposition, we primarily consider the load balance among processors. Therefore, in our computation, the subdomains are grouped from the trachea to the peripheral airways, controlling the numbers of grouped subdomains so that they are nearly equal. For example, the domain decomposition for eight-processor computation is shown in Figure 7.

We compared the performance of entirely multi-GPU computation with that of multi-CPU computation. The tests were performed on TSUBAME 1.2, a supercomputer system at the Tokyo Institute of Technology, using the airway model constructed in Section 3. The system has 657 nodes of AMD Opteron CPUs (total 10,512 cores), of which 170 nodes are connected to nVIDIA Tesla S1070 GPU devices. All of the nodes are connected with InfiniBand. The effective performances of multi-GPU and multi-CPU computations are shown in Figure 8(a). We found that about 800 CPU cores must be recruited for performance that equals eight-GPU computations. The scalability of the GPU computation peaks at eight GPUs, while the CPU computation peaks at 32 CPU cores. This indicates that the time required for data transfer cannot fully overlap with other processes in computations involving more than 16 GPUs. Taking the opposite view,

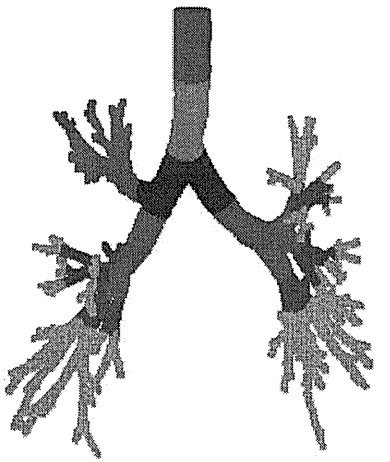

Figure 7. Domain decomposition for eight-processor computation. The subdomains shown in the same colour were computed using the same processor.

eight GPUs are sufficient to compute pulmonary airflow consisting of 12 million mesh components.

The same computation was performed on a small cluster involving eight personal computers, each mounting the latest quad-core CPU, Intel Core i7-930, and the latest GPU, nVIDIA GeForce GTX 480. GeForce GTX 480 is connected to the GDDR5 device memory, which has a bandwidth of 177.4 GB/s, whereas Core i7-930 is connected to triple-channel DDR3-1066 host memory, which has a bandwidth of 25.6 GB/s. All computers are connected using a 40-Gbps QDR InfiniBand. This cluster costed less than $30,000 in the spring of 2010 and occupies a footprint of 0.7 m^3, so it could be installed in medical offices. The result of the benchmark test is shown in Figure 8(b), which shows that high-performance computation can also be performed on personal-use GPUs. Figure 8(b) plots the effective performance for GPU computation and real performance for CPU computation, assuming that it may not be necessary to apply the developed adaptive meshing method, which includes unnecessary mesh components, in the CPU computation. Nonetheless, comparing the effective performance of GPUs with the real performance of CPUs, the result shows that 170 CPU cores, which are nearly equal to 42 quad-core CPUs, are needed to attain the performance of eight GPUs, even if the CPU computation could attain scalability. As the LBM handles 23 variables in each lattice component, particle distributions moving

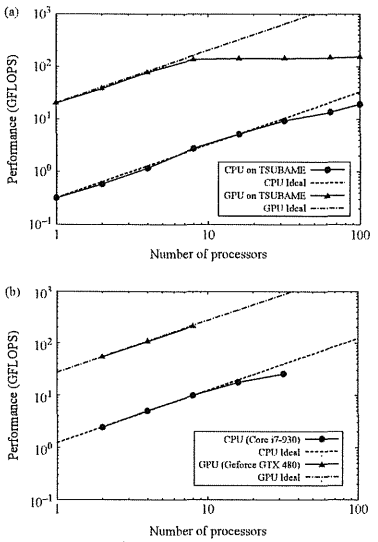

Figure 8. Benchmark test: multi-CPU vs. multi-GPU: (a) benchmark on TSUBAME 1.2 and (b) benchmark on a small cluster system.

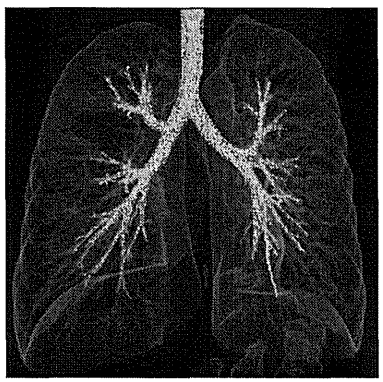

Figure 9. Particles are tracked along airflow streamlines, and the data are overlapped with volume rendered lung data from the same subject.

in 19 directions, three-dimensional velocity and density, an advantage exists on using GPUs connected to a very wide-bandwidth device memory. A simulation of inspiratory airflow is shown in Figure 9, in which particles are tracked along airflow streamlines, and the data are overlapped with a volume rendered lung data generated from the same subject. Freitas and Schröder (2008) reported a large-scale pulmonary airflow simulation using the LBM on a supercomputer system in the Jülich supercomputing centre. They used a mesh with 12 million components for the simulation, almost identical to the number we used; such a computation can be performed on a small GPU cluster using our LBM solver.

5. Conclusions

We proposed a novel approach for the patient-specific modelling of pulmonary airflow. The computational time is a major issue in the application of patient-specific models to medical practice. To overcome this problem, we developed an LBM flow solver for the use on GPU clusters. The LBM is a fully explicit solver free of the convergence problem of pressure Poisson equations encountered in semi-implicit methods. Moreover, high-performance computation can be achieved on a GPU with a wide-bandwidth device memory because the performance of the LBM depends strongly on the memory access speed. As adequate memory usage is essential for GPU computation, we also developed an adaptive meshing method for the complex pulmonary airway model. In this method, the airway model is covered by small isotropic subdomains consisting of a Cartesian mesh. The computational mesh can be generated directly from CT data, as the data consist of voxels aligned in Cartesian coordinates. We demonstrated that 4^3 size subdomains perform the best for patient-specific models of up to 13-generation airways. We confirmed that the proposed model with 12 million mesh components has scalability up to eight GPUs on TSUBAME 1.2, which are sufficient for simulating this model, while more than 800 CPU cores are needed to obtain the same results, even if the CPU could retain its scalability. The computation can also be performed on a small personal-use GPU cluster within a reasonable price and footprint. Eighty minutes is required to simulate the airflow for 1 s, or 5 h to obtain the results for one 4-s cycle of respiration, which would be reasonable for practical use in clinical diagnosis.

We will be able to analyse gas exchange phenomena or nanoparticle deposition in the airways simply by coupling advection–diffusion equations or the Lagrangian tracking of particles with this method. Such an analysis will provide useful supporting information for diagnosis and treatment. Although the GPU computation shows potential for CFD problems, an application to complex geometry problems has not been fully developed. This is a particularly crucial

issue in biomedical engineering because almost all organs have complex geometries. Our method can be applied to any complex geometry problem, such as the patient-specific modelling of blood flow. We hope that this method will lead to the efficient use of patient-specific models in a variety of medical applications.

References

Balásházy I, Hofmann W. 1993a. Particle deposition in airway bifurcations – I. Inspiratory flow. J Aerosol Sci. 24(6): 745–772.

Balásházy I, Hofmann W. 1993b. Particle deposition in airway bifurcations – II. Expiratory flow. J Aerosol Sci. 24(6): 773–786.

Comeford A, Förster C, Wall WA. 2010. Structured tree impedance outflow boundary conditions for 3D lung simulations. J Biomech Eng. 132:081002.

Corrigan A, Camelli FF, Löhner R, Wallin J. 2010. Running unstructured grid-based CFD solvers on modern graphics hardware. Int J Numer Meth Fluids. 66(2):221–229.

CUDA C best practices guide. [cited 2010 Sep 20]. Available from: http://developer.nvidia.com/

CUDA C programming guide. [cited 2010 Sep 20]. Available from: http://developer.nvidia.com/

De Backer JW, Vos WG, Devolder A, Verhulst SL, Germonpré P, Wuyts FL, Parizel PM, De Backer W. 2008. Computational fluid dynamics can detect changes in airway resistance in asthmatics after acute bronchodilation. J Biomech. 41: 106–113.

De Backer JW, Vos WG, Vinchurkar SC, Claes R, Drollmann A, Wulfrank D, Parizel PM, Germonpré P, De Backer W. 2010. Validation of computational fluid dynamics in CT-based airway models with SPECT/CT. Radiology. 257:854–862.

Freitas RK, Schröder W. 2008. Numerical investigation of the three-dimensional flow in a human lung model. J Biomech. 41:2446–2457.

Gemci T, Ponyavin V, Chen Y, Chen H, Collins R. 2008. Computational model of airflow in upper 17 generations of human respiratory tract. J Biomech. 41:2047–2054.

Kuznik F, Obrecht C, Rusaouen G, Roux J. 2010. LBM based flow simulation using GPU computing processor. Comput Math Appl. 59:2380–2392.

Lin CL, Tawhai MH, McLennan G, Hoffman EA. 2007. Characteristics of the turbulent laryngeal jet and its effect on airflow in the human intra-thoracic airways. Respir Physiol Neurobiol. 157:295–309.

Nowak N, Kakade PP, Annapragada AV. 2003. Computational fluid dynamics simulation of airflow and aerosol deposition in human lungs. Ann Biomed Eng. 31:374–390.

Palabos., [cited 2010 Sep 20]. Available from: http://www.lbmethod.org/palabos/

Qian YH, D'Humières D, Lallemand P. 1992. Lattice BGK models for Navier-Stokes equation. Europhys Lett. 17(6): 479–484.

Riegel E, Indinger T, Adams NA. 2009. Implementation of a lattice-Boltzmann method for numerical mechanics using the nVIDIA CUDA technology. CSRD. 23:241–247.

Rochefort L, Vial L, Fodil R, Mâtre X, Louis B, Isabey D, Caillibotte G, Thiriet M, Bittoun J, Durand E, et al. 2007. *In vitro* validation of computational fluid dynamic simulation in human proximal airways with hyperpolarized ^{3}He magnetic resonance phase-contrast velocimetry. J Appl Physiol. 102:2012–2023.

Stürmer M, Götz J, Richter G, Dörfler A, Rüde U. 2009. Fluid flow simulation on the cell broadband engine using the lattice Boltzmann method. Comput Math Appl. 58:1062–1070.

Thibault JC, Senocak I. 2010. Accelerating incompressible flow computations with a Pthreads-CUDA implementation on small-footprint multi-GPU platforms. J. Supercomput (Published online).

Tölke J. 2010. Implementation of a lattice Boltzmann kernel using the compute unified device architecture developed by nVIDIA. Comput Visual Sci. 13:22–39.

van Ertbruggen C, Hirsch C, Paiva M. 2005. Anatomically based three-dimensional model of airways to simulate flow and particle transport using computational fluid dynamics. J Appl Physiol. 98:970–980.

Yang XL, Liu Y, Luo HY. 2006. Respiratory flow in obstructed airways. J Biomech. 39:2743–2751.

Yin Y, Choi J, Hoffman EA, Tawhai MH, Lin CL. 2010. Simulation of pulmonary air flow with a subject-specific boundary condition. J Biomech. 43:2159–2163.

Zhang Z, Kleinstreuer C, Donohue JF, Kim CS. 2005. Comparison of micro- and nano-size particle depositions in a human upper airway model. J Aerosol Sci. 36:211–233.

Zhao Y. 2008. Lattice Boltzmann based PDE solver on the GPU. Visual Comput. 24:323–333.

Age-Related Changes in Topological Organization of Structural Brain Networks in Healthy Individuals

Kai Wu,[1]* Yasuyuki Taki,[1,2] Kazunori Sato,[1] Shigeo Kinomura,[1] Ryoi Goto,[1] Ken Okada,[1] Ryuta Kawashima,[2,3] Yong He,[4,5] Alan C. Evans,[5] and Hiroshi Fukuda[1]

[1]*Department of Nuclear Medicine and Radiology, Institute of Development, Aging and Cancer, Tohoku University, Sendai, Japan 980-8575*
[2]*Division of Developmental Cognitive Neuroscience, Institute of Development, Aging and Cancer, Tohoku University, Sendai, Japan 980-8575*
[3]*Department of Functional Brain Imaging, Institute of Development, Aging and Cancer, Tohoku University, Sendai, Japan 980-8575*
[4]*State Key Laboratory of Cognitive Neuroscience and Learning, Beijing Normal University, Beijing, China 100875*
[5]*McConnell Brain Imaging Centre, Montreal Neurological Institute, McGill University, Montreal, QC, Canada H3A 2B4*

Abstract: The aim of this study was to examine structural brain networks using regional gray matter volume, as well as to investigate changes in small-world and modular organization with normal aging. We constructed structural brain networks composed of 90 regions in young, middle, and old age groups. We randomly selected 350 healthy subjects for each group from a Japanese magnetic resonance image database. Structural brain networks in three age groups showed economical small-world properties, providing high global and local efficiency for parallel information processing at low connection cost. The small-world efficiency and node betweenness varied significantly and revealed a U- or inverted U-curve model tendency among three age groups. Results also demonstrated that structural brain networks exhibited a modular organization in which the connections between regions are much denser within modules than between them. The modular organization of structural brain networks was similar between the young and middle age groups, but quite different from the old group. In particular, the old group showed a notable decrease in the connector ratio and the intermodule connections. Combining the results of small-world efficiency, node betweenness and modular organization, we concluded that the brain network changed slightly, developing into a more distributed organization from young to middle age. The organization eventually altered greatly, shifting to a more localized organization in old age. Our findings provided quantitative insights into topological principles of structural brain networks and changes related to normal aging. *Hum Brain Mapp 33:552–568, 2012.* © 2011 Wiley Periodicals, Inc.

Key words: structural brain network; economical small-world; modular organization; normal aging; regional gray matter volume; magnetic resonance imaging

Additional Supporting Information may be found in the online version of this article.

Contract grant sponsor: 2007 Tohoku University Global COE Program "Global Nano-Biomedical Engineering Education and Research Network Centre"; the MEXT Grant-in-Aid for Scientific Research on Innovative Areas, 22103501.

*Correspondence to: Kai Wu, Institute of Development, Aging and Cancer, Tohoku University, Sendai, Japan 980-8575. E-mail: kaiwu@idac.tohoku.ac.jp

Received for publication 28 September 2009; Revised 24 October 2010; Accepted 18 November 2010

DOI: 10.1002/hbm.21232

Published online 9 March 2011 in Wiley Online Library (wileyonlinelibrary.com).

INTRODUCTION

New advances in the quantitative analysis of complex networks, based largely on graph theory, have been rapidly applied to studies of brain network topological organization. The structural and functional systems of the human brain show topological properties of complex networks, such as small-world properties, highly connected hubs, and modularity [Bullmore and Sporns, 2009]. Significant discoveries related to human brain functional networks have indicated that the brain exhibits small-world properties characterized by a high clustering index and a short average distance between any two regions [Latora and Marchiori, 2001; Watts and Strogatz, 1998], using modern neuroimaging techniques such as functional magnetic resonance imaging (fMRI), and electroencephalogram (EEG) [Achard and Bullmore, 2007; Achard et al., 2006; Bassett et al., 2006; Eguiluz et al., 2005; Ferri et al., 2007; Micheloyannis et al., 2006; Salvador et al., 2005]. It has been verified that structural networks of the human brain revealed by measurements of cortical thickness or regional gray matter volume (RGMV) have small-world properties [Bassett et al., 2008; He et al., 2007, 2008, 2009a]. Moreover, the small-world properties were confirmed in human brain structural networks using diffusion MRI technique [Gong et al., 2009b; Hagmann et al., 2007; Iturria-Medina et al., 2008]. Achard and Bullmore were the first to demonstrate economical small-world properties in brain functional networks, which provide high global and local efficiency for parallel information processing at a low wiring cost [Achard and Bullmore, 2007]. Efficiency metrics have also provided a new measure to quantify differences between patient groups and appropriate comparison groups [He et al., 2009a; Liu et al., 2008; Wang et al., 2009b].

Modularity is thought to be one of the main organizing principles in most complex systems, including biological, social, and economical networks [Girvan and Newman, 2002; Guimerà et al., 2005; Hartwell et al., 1999; Newman, 2006a]. A key advantage of modular organization is that it favors evolutionary and developmental optimization of multiple or changing selection criteria: a modular-organized network can evolve or grow one module at a time, without risking loss of function in other modules [Kashtan and Alon, 2005; Redies and Puelles, 2001]. Defining and characterizing modular organization in the human brain can help us to identify a set of modules structurally or functionally associated with components that perform specific biological functions. This investigation will also provide us with rich quantitative insights into structural–functional mapping. The modular organization of structural and functional networks in human brain has been demonstrated by several previous studies [Chen et al., 2008; Ferrarini et al., 2009; Hagmann et al., 2008; He et al., 2009b; Meunier et al., 2009a,b; Robinson et al., 2009; Valencia et al., 2009].

Normal processes of brain maturation and senescence might be reflected as quantifiable changes in structural and functional network topological properties [Bullmore and Sporns, 2009; Micheloyannis et al., 2009]. A previous study on functional brain networks indicated that an older age group had significantly reduced cost efficiency in comparison to a younger group [Achard and Bullmore, 2007]. Normal aging might thus be associated with changes in the economical small-world properties of brain functional networks. Furthermore, normal aging had been proven to be associated with changes in modular organization of human brain functional networks [Meunier et al., 2009a]. A recent study reported that the organization of multiple functional brain networks shifts from a local anatomical emphasis in children to a more distributed organization in young adults [Fair et al., 2009]. The study also demonstrated that community detection by modularity optimization reveals stable communities within the graphs that are clearly different between young children and young adults [Fair et al., 2009]. A recent study also reported that the development of large-scale brain networks is characterized by weakening of short-range functional connectivity and strengthening of long-range functional connectivity, comparing the children group (7–9 years) with the young-adults group (19–22 years), [Supekar et al., 2009]. However, few studies have analyzed the influences on both small-world and modular organization with normal aging. The main purpose of this study is to clarify topological properties in structural brain networks among different age groups. We hypothesized that the economical small-world properties and the modular organization of structural brain networks would be altered with normal aging.

In the present study, we divided all healthy subjects into three groups by age. Study participants were selected from a large-scale brain MRI database of normal Japanese (1421 subjects, ages from 18 to 80 years), [Sato et al., 2003]. The structural connectivity in the human brain consisting of 90 regions was constructed by computing the correlation matrix of RGMV across subjects within each group. Efficiency metrics were applied to investigate whether structural brain networks show economical small-world attributes and whether significant differences exist in properties of brain networks among three age-specific groups. We investigated the regional nodal characteristics of brain networks and compared the between-group differences in node betweenness. Furthermore, we examined the modular organization of structural brain networks and identified several modules of the brain network in each age-specific group. To clarify differences on the modular organization of brain networks among three groups, we compared the constitution of modules and computed attributes using, for example, the connector ratio and the distribution efficiency.

MATERIALS AND METHODS

Subjects

The subjects were all community-dwelling normal Japanese subjects recruited by two projects; the Aoba Brain

TABLE I. Characteristics of the subjects

Group ID	Age range	Number of subjects	Age (mean ± SD)
Young (Y)	18–40	551 (F: 231/M: 320)	27.42 ± 6.77
		350 (F: 158/M: 192)	***27.31 ± 6.65***
Middle (M)	41–60	560 (F: 331/M: 229)	50.94 ± 5.22
		350 (F: 196/M: 154)	***51.07 ± 5.26***
Old (O)	61–80	372 (F: 198/M: 174)	68.32 ± 4.58
		350 (F: 188/M: 162)	***68.17 ± 4.03***

The italic and bold characters indicate the characteristics of 350 subjects randomly selected for each group.

Imaging Project, Sendai, Japan and the Tsurugaya Project, Sendai, Japan. The Aoba Brain Imaging Project was performed to create a database of normal Japanese brain images [Sato et al., 2003]. To perform this, we obtained 1,637 brain MR images from normal Japanese volunteers who were living in and around Sendai City, Japan. The Tsurugaya Project study is a comprehensive geriatric assessment (CGA) of the elderly population. It involved 1,179 subjects aged 70 years or older in 2002 who were living in Tsurugaya district, Sendai City, Japan. We selected 210 subjects by random sampling from subjects who would be willing to undergo brain MRI and submitted these patients to MRI. The subjects of the two projects were all healthy and had neither present illness nor a history of neurological disease, psychiatric disease, brain tumor, or head injury. Prior to the acquisition of MR images, all subjects enrolled in the two projects were interviewed by medical doctors for screening to determine whether he/she was normal and to obtain clinical data. In both projects, we excluded in advance those subjects who had past or present history of malignant tumors, head traumas, cerebrovascular diseases, epilepsy, or psychiatric diseases. After the interview, brain MR images were obtained from each subject. The MR images were inspected by two to three well-trained radiologists. Images with the following findings were excluded from this study: head injuries, brain tumors, hemorrhage, major and lacunar infarctions, and moderate to severe white matter hyperintensities. We did not exclude the images with mild spotty white matter hyperintensities.

We collected brain images of 1,483 subjects in this study (mean ± S.D.; age, 46.30 ± 16.98 years; range: 18–80 years). To investigate the topological properties and organization of structural brain networks with normal aging, we divided all subjects into three groups by age (young, 18–40 years; middle, 41–60 years; old, 61–80 years), without regard to sex. Group ID naming and characteristics of the subjects are shown in Table I.

MRI data acquisition and the use of them for the studies by Fukuda H (the last author of the study) were approved by the Institutional Review Board of Tohoku University School of Medicine. Informed consent was obtained from each subject after a full explanation of the purpose and procedures of the study, according to the Declaration of Helsinki (1991), prior to MR image scanning.

Image Acquisition

Brain images were obtained from each subject using two 0.5 T MR scanners (Sigma contour, GE-Yokogawa Medical Systems, Tokyo) with two different pulse sequences: (1) 124 contiguous, 1.5-mm thick axial planes of three dimensional T1-weighted images (spoiled gradient recalled acquisition in steady state: repetition time (TR), 40 ms; echo time (TE), 7 ms; flip angle (FA), 30°; voxel size, 1.02 mm × 1.02 mm × 1.5 mm); (2) 63 contiguous, 3 mm-thick axial planes of gapless (using interleaving) proton density-weighted images/T2-weighted images (dual echo fast spin echo: TR, 2,860 ms; TE, 15/120 ms; voxel size, 1.02 mm × 1.02 mm × 3 mm). T1 images were used for the present analysis and all three images were used to exclude those MRIs with abnormalities, as described above.

Measurements of Regional Gray Matter Volume

After the image acquisition, RGMV for each subject was measured by using statistical parametric mapping 2 (SPM2) (Wellcome Department of Cognitive Neurology, London, UK) [Friston et al., 1995] in Matlab (Math Works, Natick, MA). First, T1-weighted MR images were transformed to the same stereotactic space by registering each of the images to the ICBM 152 template (Montreal Neurological Institute, Montreal, Canada), which approximates the Talairach space [Jean Talairach, 1988]. Then, tissue segmentation from the raw images to the gray matter, white matter, cerebrospinal fluid space, and non-brain tissue was performed using the SPM2 default segmentation procedure. We applied these processes using the MATLAB file "cg_vbm_optimized" (http://dbm.neuro.uni-jena.de/vbm.html). WFU_PickAtlas software was employed to label the regions in the gray matter images, which provided a method for generating ROI masks based on the Talairach Daemon database [Lancaster et al., 2000; Maldjian et al., 2003, 2004]. We parcellated the entire gray matter into 45 separate regions for each hemisphere (90 regions in total, see Supporting Information Table SI) defined by the Automated Anatomical Labeling (AAL) atlas [Tzourio-Mazoyer et al., 2002] to calculate the RGMV for each subject.

Construction of Brain Structural Connection Matrix

To study the topological properties of structural brain networks among three age-specific groups, we examined the correlation matrices using graph-theoretical analysis: GroupIDs were Young, Middle, and Old. Since there was a large difference in the number of subjects in each group, we randomly selected 350 subjects for each age group (the original group) (Table I) to reduce the influence due to varying degrees of freedom for each group in computing inter-regional correlation across subjects. We also repeated this randomly-selected grouping method 20 times in each age group to examine whether subject characteristics were

TABLE II. Topological parameters of structural brain networks used in this study

Network properties	Characters	Descriptions
Economical small-world properties	Cost	The cost or the sparsity to construct a network.
	Eloc	The local efficiency measures how efficient are the network to exchange the information at the clustering level.
	Eglob	The global efficiency measures how efficient are the network to exchange the information at the global level.
	I_{Eloc}	The integrated local efficiency is the integrals of the local efficiency curves over the preselected range of cost threshold.
	I_{Eglob}	The integrated global efficiency is the integrals of the global efficiency curves over the preselected range of cost threshold.
Nodal characteristics	BC	The normalized betweenness measures the ability of a node relative to information flow between other nodes throughout the network.
	I_{BC}	The integrated normalized betweenness is the integrated normalized betweenness over the preselected range of cost threshold.
Modularity	B	The modularity measures how the network is organized into modules with high level of local clustering.
	sBC	The within-module betweenness centrality measures the importance of a node relative to the information flow between other nodes in the module.
	PC	The participant coefficient measures the ability of a node to maintain the communication between its own module and the other modules.

significantly changed. As a result, the characteristics of 350 subjects randomly selected for each age group were not significantly different from those of the original group. We used a linear regression analysis to remove the effects from total gray matter volume and sex, so that the residuals of this regression were employed as the substitute for the raw RGMV, denoted as corrected RGMV (cRGMV). To analyze the structural brain network by using RGMV, we first applied the method introduced by He et al. to construct the structural connection matrix [He et al., 2007]. We computed the Pearson correlation coefficient between cRGMV across 350 subjects randomly chosen from each group to construct the interregional correlation matrix ($N \times N$, where N is the number of gray matter regions, here $N = 90$) for each group. Each connection matrix can be converted to a binarized and undirected graph (network) G by using a correlation or cost threshold. Then the networks were analyzed by using graph theoretical methods. All topological parameters of the networks calculated in this study and their implications are shown in Table II.

Small-World Properties

Small-world properties (clustering coefficient, C_p and characteristic path length, L_p) were originally defined by Wattz and Strogatz [1998]. In addition to the conventional small-world parameters (C_p and L_p), more biologically sensible properties of brain networks are the efficiency metrics (global efficiency, E_{glob} and local efficiency, E_{loc}), which measure the capability of the network with regard to information transmission at the global and local levels, respectively [Latora and Marchiori, 2001]. In several recent studies, the efficiency metrics have been applied to human brain functional [Achard and Bullmore, 2007; Wang et al., 2009a,b] and structural [He et al., 2009a; Iturria-Medina et al., 2008] network studies. For a graph G with N nodes and K edges, the global efficiency of G can be computed as [Latora and Marchiori, 2001]:

$$E_{\text{glob}}(G) = \frac{1}{N(N-1)} \sum_{i \neq j \in G} \frac{1}{d_{ij}} \quad (1)$$

where d_{ij} is the shortest path length between node i and node j in G. The local efficiency of G is defined as [Latora and Marchiori, 2001]:

$$E_{\text{loc}}(G) = \frac{1}{N} \sum_{i \in G} E_{\text{glob}}(Gi) \quad (2)$$

where $E_{\text{glob}}(G_i)$ is the global efficiency of G_i, the sub-graph of the neighbors of node i. In this study, we generated a population (n 1,000) of regular networks and random networks that preserved the same number of nodes and edges, respectively. The efficiency metrics (E_{glob} and E_{loc}) of real brain networks (G) were compared with those of regular graphs (G_{reg}) and random graphs (G_{rand}), respectively. The real brain network G is considered to be a small-world network if it meets the following criteria [Latora and Marchiori, 2001]:

$$E_{\text{glob}}(G_{\text{reg}}) < E_{\text{glob}}(G) < E_{\text{glob}}(G_{\text{rand}}) \text{ and } E_{\text{loc}}(G_{\text{rand}}) < E_{\text{loc}}(G) < E_{\text{loc}}(G_{\text{reg}}) \quad (3)$$

In this study, we applied a cost threshold to investigate economical small-world properties of networks. Such a thresholding approach can normalize all networks to have

the same number of edges or wiring cost and thus provide an avenue to detect changes in topological organization with aging [Achard and Bullmore, 2007; He et al., 2009a]. To estimate the small-world properties of structural brain networks and to define a small-world regime, we first applied a broad cost threshold range ($0.05 \leq$ cost ≤ 0.5, increased by 0.01) to all the connection matrices. The cost (or sparsity) was computed as the ratio of the number of actual connections divided by the maximum possible number of connections in the network. We then adopted the following complementary approaches to choose the small-world regime: (1) the small-world properties were estimable ($K > \log(N) = 4.5$, $N = 90$) [Watts and Strogatz, 1998], (2) all brain networks were fully connected, and (3) the resulting brain networks have sparse properties and distinguishable properties in comparison to the degree-matched random networks [Bassett et al., 2008; Liu et al., 2008; Wang et al., 2009a]. Finally, we selected the small-world regime as a range of cost threshold ($0.11 \leq$ cost ≤ 0.25, step $= 0.01$). These thresholds were also used for the following calculation of regional nodal characteristics and modularity.

Regional Nodal Characteristics

In this study, we examined the node betweenness in the networks. The betweenness bc_i of a node i is defined as the number of shortest paths between any two nodes that run through node i [Freeman, 1977]. We defined the normalized betweenness as $BC_i = bc_i/\langle bc_i \rangle$, where $\langle bc_i \rangle$ was the average betweenness of all nodes. Thus, the normalized betweenness of BC_i measures the ability of a node relative to information flow between other nodes throughout the network. Finally, we averaged the normalized betweenness across the range of cost threshold ($0.11 \leq$ cost ≤ 0.25). Regions with a higher value of $\overline{BC}_i$ (> mean + SD) were identified as global hubs in the brain network [Sporns et al., 2007].

Modularity and Regional Role

A module can be generally defined as a subset of nodes in the graph that are more densely connected to the other nodes in the same module than to nodes outside the module [Radicchi et al., 2004]. Several algorithms have been proposed to define the modular decomposition of an undirected graph [Clauset et al., 2004; Danon et al., 2005; Guimerà and Amaral, 2005a, 2005b; Guimerà et al., 2004; Newman 2006a, 2006b, 2004; Newman and Girvan, 2004; Reichardt and Bornholdt, 2006]. Despite the many interesting alternative methods, it should be noted that the problem of community finding remains a challenge because no single method is fast and sensitive enough to ensure ideal results for general, large networks, a problem that is compounded by the lack of a clear definition of communities. Here, we adopted the spectral algorithm [Guimerà and Amaral, 2005b; Guimerà et al., 2004; Newman, 2006a] for community detection, which is believed to be the most precise and be able to find a division with the highest value of modularity for many networks [Costa et al., 2007]. This algorithm reformulates the modularity concept in terms of the eigenvectors of a new characteristic matrix for the network, called the modularity matrix [Newman, 2006a].

For each subgraph g, its modularity matrix $B^{(g)}$ has elements

$$b_{ij}^{(g)} = a_{ij} - \frac{k_i k_j}{2M} - \delta_{ij} \sum_{u \in N(g)} \left[a_{iu} - \frac{k_i k_u}{2M} \right] \quad (4)$$

for vertices i and j in g. In Eq. (4), the actual number of edges falling between a particular pair of vertices i and j is aij; k_i is the degree of a vertex i; $\delta_{ij} = 1$ if $i = j$ and 0 otherwise. Thus, to split the network in communities, the modularity matrix is constructed and its most positive eigenvalue and corresponding eigenvector are determined. According to the signs of the elements of this vector, the network is divided in two parts (vertices with positive elements are assigned to one community and vertices with negative elements to another). Next, the process is repeated recursively to each community until a split that makes a zero or negative contribution to total modularity is reached. Similarly, Newman proposed a new definition of communities as indivisible subgraphs, i.e., subgraphs whose division would not increase the modularity.

In this study, we detected the community structure for the structural brain networks of three groups, which were thresholded by a specific cost threshold (cost = 0.11). With this threshold, we can capture the structural connectivity backbone underlying the modular organization of the most sparse and fully-connected brain networks. To further distinguish the roles of nodes in terms of their intra- and inter-module connectivity patterns, the two measurements, the within-module betweenness centrality, sBC and the participant coefficient (PC) were applied [Guimerà and Amaral, 2005a; Guimerà et al., 2005]. The sBC (i) of a node i is the betweenness centrality, but is calculated only within the module s to which it belongs. This parameter measures the importance of a node relative to the information flow between other nodes in the module. The PC(i) of a node i is defined as

$$PC(i) = 1 - \sum_{s=1}^{N_M} \left(\frac{k_{is}}{k_i} \right)^2$$

where N_M is the number of modules, k_{is} is the number of links of node i to nodes in module s and k_i is the total degree of node i. The PC(i) tends to 1 if node i has a homogeneous connection distribution with all the modules and to 0 if it does not have any inter-module connections. PC measures the ability of a node to maintain the communication between its own module and the other modules. A high PC value for a given node usually means the node has many inter-module connections. Depending on the sBC, the nodes in the brain functional network were classified as modular hubs (sBC >mean + std) or non-hubs (sBC ≤mean + std), respectively. In terms of the PC, the hub nodes were further subdivided into R1 connector hubs (PC > 0.25) and R2 provincial hubs (PC ≤ 0.25), and non-hub nodes were divided into R3 connector non-hubs (PC > 0.25) and R4 peripheral non-hubs (PC ≤ 0.25) [Guimerà and Amaral, 2005a; Guimerà, 2005].

Statistical Analysis

To analyze statistical significance of between-group differences with regard to the efficiency metrics (local and global efficiency) among three age-specific groups, a non-parametric permutation test method was applied in the small-world regime defined above ($0.11 \leq$cost ≤ 0.25, step $= 0.01$), [Bullmore et al., 1999; He et al., 2008]. Thus, we can explore the between-group differences in efficiency metrics at each threshold level. Here, we performed three comparisons (Z_I, Z_{II}, Z_{III}) including the young versus middle (Y vs. M), the middle versus old (M vs. O), and the young versus old (Y vs. O), respectively. For each comparison, the efficiency metrics of binarized graphs at a given threshold were computed separately for each group. Then one randomization procedure of the permutation test yielded two new groups that were generalized by randomly reallocating each subject's set of cRGMV measures from previous groups. The correlation matrices for new groups were recomputed and binarized by thresholding to achieve the same threshold as in the real networks. The efficiency metrics of corresponding binarized graphs and their between-group differences were calculated. This permutation test randomization procedure was repeated 1,000 times at each threshold, consistent with the real networks. Finally, the 95th percentile points of each distribution were used as the critical values for a one-tailed test of the null hypothesis with a probability of Type I error of 0.05. Moreover, we calculated the integrals of the efficiency metrics curves as the integrated metrics (I_{Eloc}, the integrated local efficiency; I_{Eglob}, the integrated global efficiency) over the preselected range of cost threshold. Between-group significances of three comparisons on the integrated metrics were also estimated by 1,000 permutation tests. For the investigation of node betweenness, we also computed the between-group significance of two comparisons (Y vs. M and M vs. O) on the integrated normalized betweenness (I_{BCi}) over the cost threshold range, using 1,000 permutation tests. To adjust for the multiple comparisons, a false discovery rate (FDR) procedure was applied at a q value of 0.05 [Genovese et al., 2002]. We also calculated the ratio of intermodule connections under a cost threshold range ($0.11 \leq$ cost ≤ 0.25, step $= 0.01$) with the modular organization by the cost of 0.11. An ANOVA analysis was applied to test the between-group significance of the ratio of intermodule connections.

RESULTS

Economical Small-World Properties and Age-Related Changes

We used a range for cost threshold ($0.11 \leq$ cost ≤ 0.25, step $= 0.01$) to verify the properties of structural brain networks from three age-specific groups (Young, 18–40 years; Middle, 41–60 years; Old, 61–80 years). With the cost thresholding strategy, both the local and global efficiency curves of structural brain networks in three groups were intermediate compared with those of the matched random and regular networks (Fig. 1A,B). The structural brain networks in three age-specific groups exhibited economical small-world properties, indicated by higher local and global efficiency than comparable random and regular networks, respectively [Latora and Marchiori, 2001].

As shown in Figure 1A, the local efficiency in the young group was significantly larger than those of the middle and old groups, whereas no significant difference was found between the middle and old groups. The global efficiency of the young group was significantly lower than that of the middle and old groups, and the old group had significant lower values than the middle group (Fig. 1B). Using the integrated efficiency metrics over the small-world regime, we defined a U-curve model to clarify the trend of topological properties of structural brain networks with normal aging. The integrated local and global efficiency showed a U-curve and an inverted-U-curve, respectively (Fig. 1C,D).

Regional Nodal Characteristics and Age-Related Changes

To identify the global hubs in structural brain networks, we averaged the normalized node betweenness centrality BC_i of each region over the cost threshold regime. The regions with higher $\overline{BC}_i$ (> mean + sd) were identified as the global hubs (Table III). In the young group, 16 regions were designated as the global hubs, specifically 14 association regions and 2 limbic/paralimbic regions. In the middle group, 14 regions were identified as the global hubs, specifically 10 association regions and 4 limbic/paralimbic regions. In the old group, 14 regions were identified as the global hubs, specifically 10 association regions, 3 limbic/paralimbic regions and 1 subcortical region. Among the identified global hubs, 12 of 16 regions in the young group, 9 of 14 regions in the middle group, and 7 of 14 regions in the old group were frontal and parietal regions. Results also indicated that 10 out of all 14 global hubs in the middle group and 6 out of all 14 global hubs in the old group were also identified as the global hubs in the young group. To further clarify the alteration of regional

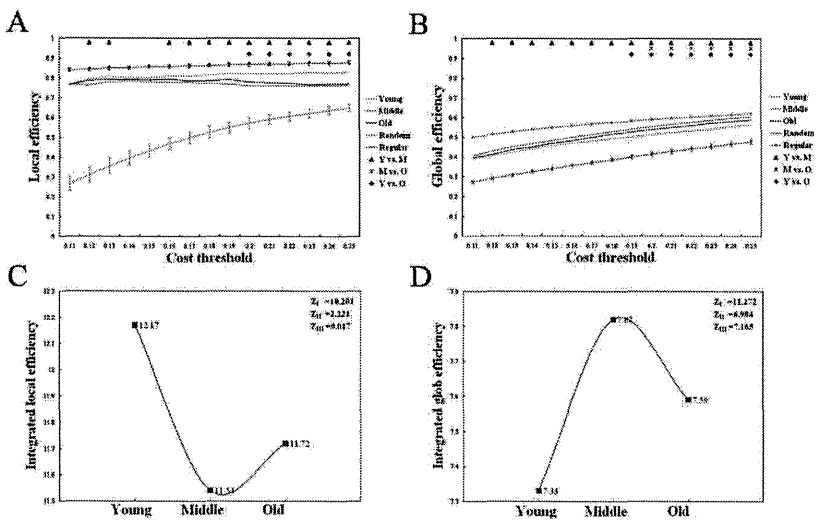

Figure 1.

Economical small-world properties and age-related changes. Left: The local and global efficiency of brain networks as a function of cost threshold. Right: The trend for the integrated efficiency metrics in age-specific groups. **A**: Local efficiency calculated under the cost threshold range of 0.11–0.25. **B**: Global efficiency calculated under the cost threshold range of 0.11–0.25. Significant differences between age groups were tested by permutation test under uncorrected conditions ($P < 0.05$). ▲: Y vs. M, ×; Y vs. M, ◆; Y vs. O. **C**: Integrated local efficiency. **D**: Integrated global efficiency. Three comparisons were performed as follows: Z_I (Young vs. Middle), Z_{II} (Middle vs. Old), and Z_{III} (Young vs. Old).

nodal characteristics, we applied 1,000 permutation tests to compute the significance of between-group differences in node betweenness ($P < 0.001$, FDR-corrected). The results indicated that six regions in the dorsal frontal-parietal junction [IFGoperc.L, SFGmed.L, SFGmed.R, SFGdor.L, IPL.L, PCUN.L; for abbreviation see Supporting Information Table SI] showed decreased node betweenness from young to middle age, whereas only three regions in the ventral frontal and temporal lobes [ORBinf.L, ORBinf.R, STG.L] revealed increased node betweenness (see Supporting Information Table SII). For the period from middle to old age, five ventral lateral cortices in the frontal and temporal lobes [ORBinf.L, ORBinf.R, ORBmed.R, MTG.L, MTG.R] showed decreased node betweenness, whereas nine regions mostly in the lateral occipital-parietal junction [MOG.L, MOG.R, ANG.L, ANG.R] and the paralimbic/subcortical area [PHG.R, AMYG.R, CAU.L, THA.L] revealed increased node betweenness (see Supporting Information Table SIII). The global hubs and the significant age-related changes in node betweenness were visualized by surface representations of structural brain networks using the Caret software [Van Essen, 2005], (see Fig. 2).

Modularity and Age-Related Changes

Maximum modularity (M) of brain networks decreased as a function of increasing cost threshold (see Supporting Information Fig. S1). It is generally accepted that $M \geq 0.3$ are indicative of nonrandom community structure [Newman and Girvan, 2004]. In this study, as the values of modularity were all larger than 0.3 over the preselected cost threshold range, and structural brain networks were consistently modularly organized in three age groups. However, there was no significant difference in modularity

TABLE III. The global hubs of the structural brain networks

		Young			Middle			Old			
Abbreviations	Class	N_{bc}(i)	Module	Role	N_{bc}(i)	Module	Role	N_{bc}(i)	Module	Role	Reference
SFGmed. L	Association	4.559	IV	R2				4.762	IV	R3	E
MTG. L	Association	4.305	V	R3	3.543	V	R3				B, C, E, F, G
SFGmed. R	Association	3.698	IV	R4							A, C, D, E
MOG. R	Association	3.569	I	R3				2.737	II	R3	A, G
ORBmed. R	Paralimbic	2.876	V	R3	3.451	V	R3				
LING. R	Association	2.865	III	R3	1.945	II	R3				B, G
SMG. L	Association	2.846	I	R3	2.579	I	R3	1.997	I	R3	B
SMG. R	Association	2.496	III	R3	1.853	IV	R3	2.249	I	R3	C
PCUN. L	Association	2.442	III	R3							A, D, G
IFGtriang. R	Association	2.321	I	R3	2.610	I	R3	2.999	I	R3	E, G
ORBmed. L	Paralimbic	2.289	V	R3	2.009	V	R3				C
SFGdor. L	Association	2.261	IV	R2							A, D, E, G
MTG. R	Association	2.162	V	R3	3.631	V	R3				B, C, E, F, G
IFGtriang. L	Association	2.086	I	R3	1.854	I	R3	2.689	I	R3	E, G
PCUN. R	Association	2.050	III	R1							A, D, G
SFGdor. R	Association	2.028	IV	R4	1.941	IV	R2				A, C, D, E, F, G
ANG. R	Association							3.431	II	R3	B
AMYG. R	Paralimbic							3.389	V	R3	
PHG. R	Paralimbic							2.760	V	R2	E, F
STG. R	Association				2.986	I	R3	2.665	I	R4	B, C, G
ANG. L	Association							2.318	II	R3	B
INS. L	Paralimbic							2.211	I	R2	D
MOG. L	Association							2.016	II	R3	A, G
THA. L	Subcortical							1.948	I	R3	
STG. L	Association				1.991	I	R1				B, G
ORBinf. L	Paralimbic				3.037	V	R1				B, C
ORBinf. R	Paralimbic				3.018	V	R3				B

The hub regions (normalized node betweenness, Nbc(i)>mean + SD) in structural brain networks of three age groups are listed in decreasing order of the node betweenness in the young group. The regions are classified as association, primary, limbic/paralimbic or subcortical regions as described by Mesulam [2000]. The module column indicates the anatomical modules that the hub regions belong to, and the role column indicates the roles that the hub regions play in terms of their intra- and inter-module connectivity patterns; connector hub (R1), provincial hub (R2), connector non-hub (R3), and provincial non-hub (see Materials and Methods). R: right; L: left. For the description of the abbreviations, see supplementary Table S1.

The reference column indicates the hub regions previously identified in human brain structural (A, B, C, D, E), or functional (F, G) networks. A; Gong et al. [2009], B; He et al. [2008], C; Chen et al. [2008], D; Iturria-Medina [2008], E; He et al. [2007], F; He et al. [2009b], G; Achard et al. [2006].

among the age-specific groups. Using the fixed cost threshold (cost = 0.11), the obtained brain networks that captured the structural connectivity backbone underlying the principal topological organization were separated into modules according to the spectral method proposed by Newman [2006a]. As a result, the brain networks were separated into five, six, and five modules in young, middle, and old groups, respectively (Table IV, see Supporting Information Table SIV). The brain regions included in modules with three age groups were described in Supporting Information Text S1. The surface representations for modules in structural brain networks are shown in Figure 3. Moreover, the modular organization of structural brain networks shown here was also reproduced by using different specific cost thresholds (cost = 0.15 and 0.20), (see Supporting Information Fig. S2). We showed the modular organization of the structural brain networks in topological spaces (Fig. 4A–C). The topological representations were drawn by the Pajek software package (http://vlado.fmf.uni-lj.si/pub/networks/pajek) using a Kamada-Kawai algorithm [Kamada Kawai, 1989]. With this algorithm, the geometric distance between two brain regions on the drawing space approximates the shortest path length between them.

In this study, according to the patterns of intra- and inter-module connections, the four possible roles of regions were defined as connector hub (R1), provincial hub (R2), connector non-hub (R3), and provincial non-hub (R4). To show the node roles of regions in each module, we arranged the connector nodes (R1 and R3) in a central ring. In the young and middle group, 49 regions (8 R1 and 41 R3) and 49 regions (7 R1 and 42 R3) were identified as connector nodes (Table IV, Fig. 4D,E). However, only 28 regions (3 R1 and 25 R3) were defined as the connectors

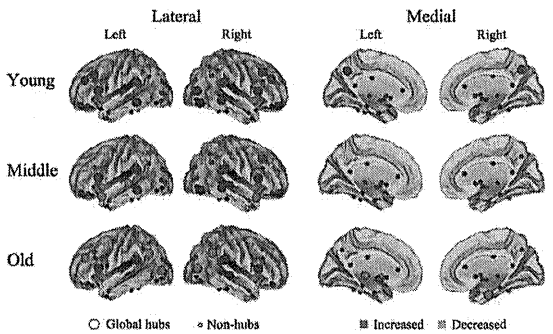

Figure 2.

Surface representations for global hubs and the significant age-related changes in node betweenness. Top: The global hubs in the young group. Middle: The global hubs in the middle group and the significant age-related changes in node betweenness from young to middle age. Bottom: The global hubs in the old group and the significant age-related changes in node betweenness from middle to old age. The global hubs and non-hubs are indicated by spheres in big and small size, respectively. The nodes with significant decreased and increased age-related changes are indicated by green and red spheres, respectively. The nodes without significant age-related change are indicated by blue spheres.

(Table IV, Fig. 4F). Most global hubs (Young, 12/16; Middle, 13/14; Old, 11/14) played R1 or R3 (connector) roles, with numerous inter-module connections executing a critical impact on the coordination of information flow through the whole network (Table III).

In addition to discrepancies in the composition and numbers of modules, we also found differences in the topological roles of the modules in the brain networks of three groups. We defined the connector-module as the module that had both a high connector ratio (the ratio of the connectors to the regions in the module was larger than 0.6) and a high ratio of intermodule connections (the ratio of the intermodule connections in the modules to that in the whole network was larger than <1/numbers of modules>) (Table IV). In both the young and the middle group, Modules I, III, and V were identified as the connector-modules (Table IV). The young brain network was observed to have dense inter-module connections between Module I and V (53/109), as well as between Module I and III (25/109) (see Supporting Information Table SV). In

TABLE IV. The distribution of connectors and inter-module connections in each module

	Young			Middle			Old		
Module	Regions	Connector	Intermodule	Regions	Connector	Intermodule	Regions	Connector	Intermodule
I	16	***11(0.69)***	***80(0.37)***	13	***9(0.69)***	***49(0.25)***	26	7(0.27)	51(0.36)
II	21	8(0.38)	16(0.07)	18	6(0.33)	25(0.13)	10	4(0.40)	43(0.30)
III	14	***12(0.86)***	***43(0.20)***	18	***12(0.67)***	***35(0.18)***	8	4(0.50)	12(0.09)
IV	20	3(0.15)	10(0.05)	19	6(0.32)	16(0.08)	18	6(0.33)	19(0.13)
V	19	***15(0.79)***	***69(0.32)***	14	***11(0.79)***	***58(0.30)***	28	3(0.11)	13(0.09)
VI				8	5(0.63)	15(0.08)			
Total number	90	49	109	90	49	99	90	24	69

The "Connector" column indicates the numbers of connector nodes in each module and its ratio to the total number of regions in the module (in parentheses). The "Intermodule" column indicates the numbers of intermodule connections in each module and its ratio to the total number of intermodule connections in the whole network (in parentheses). The bold and italic characters indicate the values of the connector-module in each age group, with both the higher connector ratio (>0.6) and the higher ratio of intermodule connections (larger than <1/number of modules>).

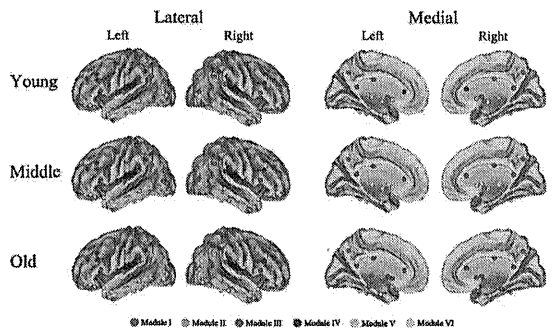

Figure 3.

Surface representations for modules in structural brain networks. All of 90 brain regions are plotted by different colored spheres (different colors represent distinct network modules) and further mapped onto the cortical surfaces at the lateral and medial views, respectively.

the middle group, the inter-module connections spread around modules and abundant connections existed only between Modules I and V (28/99) (see Supporting Information Table SVI). Although no module was recognized as the connector-module in the old group, there were relatively dense inter-module connections between Modules I and II (32/69) (see Supporting Information Table SVII). Furthermore, the young and middle groups showed significantly higher proportions of intermodule connections than did the old group (ANOVA, $P = 0.007$), (Fig. 5).

DISCUSSION

This is the first study, to our knowledge, to investigate both small-world properties and modularity of structural brain networks in healthy individuals across a broad age range. We found that structural brain networks exhibited economical small-world properties in three age-specific groups. We defined the global hubs to account for higher node betweenness in each group. In particular, the small-world properties and node betweenness showed significant changes with normal aging. Moreover, our results demonstrated that structural brain networks showed modular organization in three groups and changed greatly in the old age group. Structural brain networks developed into a more distributed organization from young to middle age, then organized into a localized organization with substantial alterations in old age. Thus, understanding changes in topological properties in structural brain networks may help elucidate normal processes of brain maturation and senescence.

Economical Small-World Properties and Age-Related Changes

In this study, structural brain networks exhibited economical small-world properties in all age-specific groups, as determined using RGMV with MR images. Our findings of high global and local efficiency in structural brain networks with three age-specific groups were compatible with previous functional and structural brain networks studies [Achard and Bullmore, 2007; Bassett et al., 2008; He et al., 2008, 2009a; Wang et al., 2009b]. Computational modeling simulations [Sporns et al., 2000] and experimental studies [Chen et al., 2008] have also suggested the emergence of small-world topology when networks are evolved for the great complexity of dynamic behavior, defined as an optimal balance between local specialization and global integration [Strogatz, 2001]. Thus, our results provided further support for the standpoint that brain networks might have evolved to maximize the cost efficiency of parallel information processing.

We also noted age-related changes in efficiency metrics of structural brain networks. First, the structural brain network may develop into a more distributed organization from young to middle age, accompanied by significant decreases in local efficiency and robust increases in global efficiency. The reduction of local efficiency might be related to that healthy aging is associated with a regionally distributed pattern of gray matter atrophy [Bergfield et al., 2010]. Moreover, a previous study suggests that high global efficiency assures effective integrity or rapid transfers of information between and across remote regions that are believed to constitute the basis of cognitive

process [Sporns and Zwi, 2004]. Recent studies also demonstrate a positive correlation between the global efficiency of brain networks and intellectual performance, indicating a more efficient parallel information transfer in the human brain [Li et al., 2009; van den Heuvel et al., 2009]. Thus, the period from young to middle age may reflect a maturation process in the structural brain network. This finding was also in accordance with that the age-related cognitive changes involved in the age-related loss of gray matter volume [Hedden and Gabrieli, 2004; Resnick et al., 2003; Tisserand et al., 2004]. Second, the structural brain network may evolve into a more local organization from middle to old age. The local efficiency did not differ significantly between the middle and old groups (Fig. 1A), whereas the integrated local efficiency increased significantly (Fig. 1C). Besides, the global efficiency and the integrated global efficiency decreased significantly (Fig. 1B,D). This phenomenon may indicate a degeneration process in the structural brain network with normal aging. It has been suggested the regular networks have a slow signal propagation speed and synchronizability in comparison to small-world networks [Strogatz, 2001]. The regular configuration that upsets the optimal balance of a small-world network was related to many neurological and psychiatric disorders described as dysconnectivity syndromes [Catani and ffytche, 2005]. Many previous studies have reported the regular configuration of brain networks in patients with diseases such as schizophrenia or AD, derived from fMRI, EEG or structural MRI data [Bassett et al., 2008; He et al., 2008; Stam et al., 2007]. There seems to be convergent evidence from methodologically disparate studies that both AD and schizophrenia are associated with abnormal topological organization of structural and functional brain networks [Bullmore and Sporns, 2009]. Thus, our results suggested that aging has high risk for dysconnectivity syndromes. Third, the U-curve model defined in this study indicated a quadratic curve-like tendency of structural brain networks with normal aging. Our recent study demonstrated that gray matter volume declined with age in healthy community-dwelling individuals, whereas the white matter ratio (WMR) had an inverted-U curve trajectory with age. WMR increased until around 50 years of age and then decreased in each gender [Taki et al., in press]. This increase in the WMR is thought to represent maturational changes such as myelination, which may continue until middle adulthood. There are other supporting evidences that both gray and white matter magnetization transfer ratio (MTR) histograms follow quadratic curves: in both cases, they increase up until middle adulthood and then decline significantly, as determined by a study that assessed age-related MTR histogram measurements in healthy subjects (54 healthy volunteers Aged 20–86 years), [Ge et al., 2002a,b]. Brain maturation includes both regressive cellular events (such as synaptic pruning) and progressive cellular events (such as myelination), which could result in the appearance of regional gray matter volume decline or cortical thinning on MR images [Sowell et al., 2003, 2004]. It has been noted that brain maturational change continues to about the fifth decade of age [Sowell et al., 2003], which may account for the maturation of structural brain networks.

In addition to the above findings, we observed that the young group showed higher local efficiency (Fig. 1A,C) but lower global efficiency (Fig. 1B,D) as compared with the old group. This finding was different from the results of a previous study [Achard and Bullmore, 2007], in which the young group (N = 15; mean age = 24.7 years) showed higher values in the relative global efficiency and no significant difference in the relative local efficiency compared with the old group (N = 11; mean age = 66.5 years). The discrepancies could be attributed to different network modalities (structural vs. functional) and population size (350 vs. 11/15).

Regional Nodal Characteristics and Age-Related Changes

Node betweenness is an important metric that can be used to determine the relative importance of a node with a network and identify the pivotal nodes in the complex network. As indicated by the higher values of node betweenness, 16, 14, and 14 global hubs that are crucial to efficient communication were identified in the young, middle, and old groups, respectively. These global hub regions were mainly composed of recently evolved association and primitive limbic/paralimbic regions. Association regions have proven to contribute to the integrity of multiple functional systems, such as attention and memory systems [Mesulam, 1998], and tend to be hubs of the brain functional network regardless of age [Achard and Bullmore,

Figure 4.

Modular organization of structural brain networks. Left: The modular organization of young (**A**), middle (**B**), and old (**C**) brain networks visualized by minimizing free energy using a Kamada-Kawaki layout algorithm. The global hubs and non-hubs are represented by the bigger and smaller circles, respectively. The regions are represented by the module color. The intramodule and intermodule connections are represented by the light gray and black lines, respectively. Right: The regional node roles in brain modules for young (**D**), middle (**E**), and old (**F**) brain networks, with connector nodes located in a central ring to highlight intermodule connections. The intramodule and intermodule connections are shown in colored and black lines, respectively.

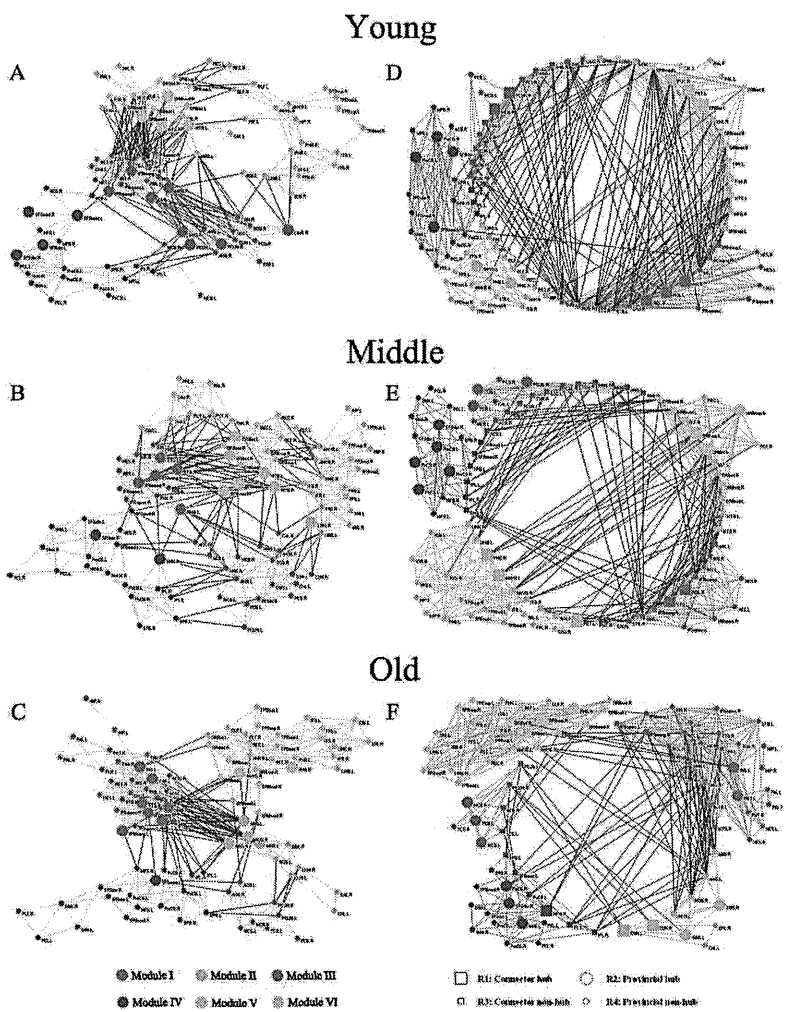

Figure 4.

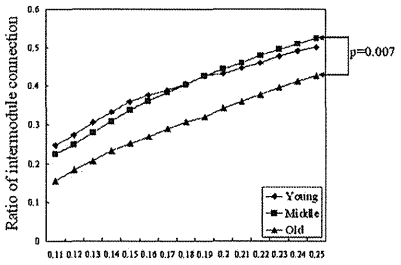

Figure 5.
The ratio of intermodule connections.

2007]. Limbic/paralimbic regions have been shown to be highly interconnected with the prefrontal regions and subcortical regions, and are mainly involved in emotional processing and the maintenance of a conscious state of mind [Mesulam, 1998]. In this study, most global hubs were frontal and parietal regions, especially in the young (12 of 16) and middle (9 of 14) groups. Previous studies have also demonstrated that identified global hubs were mainly prefrontal and parietal regions, providing a potential explanation for their well-documented activation by many cognitive functions [Bullmore and Sporns, 2009]. Moreover, although the identified global hubs varied among three age-specific groups, most of these regions were found to show high regional efficiency or node betweenness in the structural [Chen et al., 2008; Gong et al., 2009b; He et al., 2007, 2008; Iturria-Medina et al., 2008] and functional [Achard et al., 2006; He et al., 2009b] human brain networks (Table III). It was noted that the substantial discrepancies of identified global hubs between this study and the previous studies could be due to the different neuroimaging modalities, subjects' characteristics and computational methods.

We also found significant changes in node betweenness with decreasing and increasing in both periods (see Fig. 2). This finding was consistent with a previous study which indicates both negative and positive age effects on the regional efficiency in cortical regions [Gong et al., 2009a]. The most of these identified regions were association cortices (7 out of 9) in the period from young to middle age. From middle to old age, the regions were association (7 out of 14) and paralimbic/subcortical (7 out of 14) regions. These results supported the view that age-related changes are mainly characteristic of association cortex as opposed to primary cortex [Albert and Knoefel, 1994]. Our results were also similar to the result by a previous study that old age is associated with significantly reduced nodal efficiency in several regions of the frontal and temporal neocortex [Achard and Bullmore, 2007]. We also tried to interpret this phenomenon by previous results in the dynamic course of brain maturation. A previous study indicates that relative regional differences in cortical GM volume with age occur in the frontal, parietal and temporal lobes [Smith et al., 2007]. Importantly, the discrepancies in node betweenness between middle and old groups were more notable than those between young and middle groups (see Fig. 2). Thus, our results suggested that the organization of structural brain networks changed slightly from young to middle age, whereas it altered greatly from middle to old age.

Modularity and Age-Related Changes

Our results indicated the existence of modular organization in the structural brain networks in three age-specific groups. The organization consisted of modules of tightly connected brain regions. Each module in a network has intramodule connections that are denser than its intermodule connections. High local clustering represents a general organizational principle throughout many larger-scale brain networks and may contribute to the balance between brain functional segregation and integration while conserving connection length, efficient recurrent processing within modules, and efficient information exchange between modules [Bassett and Bullmore, 2006; Chen et al., 2008; Latora and Marchiori, 2001; Sporns et al., 2000]. Thus, this finding of modular organization in structural brain networks was consistent with the pre-stated results of economical small-world attributes, indicated by higher local and global efficiency than comparable random and regular networks, respectively. Moreover, we noted that the structural brain networks were organized with topological modules that closely overlap known functional domains such as auditory and language (Module I in young and middle), memory and emotion processing (Module II in young and middle), visual and "default" network (Module III in young and middle), motor and somatosensory (Module IV in young, middle, and old), cognitive processing and learning (Module V in young), and decision-making (Module V in middle). The modules in the old group were quite different from those in the young and middle groups. Specially, Module I was primarily associated with memory, as well as auditory and language functions; Module II was mainly involved in the visual system; Module III was involved with emotion formation and processing; Module V was similar to Modules II and V in the middle group, which were mainly associated with memory, emotion, and cognitive processing. These results were also in accordance with several recent studies on the modular organization of human brain that utilized structural and functional network analyses [Chen et al., 2008; Hagmann et al., 2008; He et al., 2009b]. For the full discussion, see Supporting Information Text S1.

We also found no significant difference with regard to the modularity of the global brain networks among three age-specific groups [see Supporting Information Fig. S1]. This finding was consistent with that of a previous study, in which no significant difference was found between the young and old groups with regard to modularity, implying that modular organization is conserved over the adult age range considered [Meunier et al., 2009a]. Nonetheless, there were notable discrepancies in the composition and topological roles of modules among brain networks in this study. First, comparing the composition of the modules among three age groups, we found that the modular organization of the young and middle groups were very similar but quite different from that of the old group (Figs. 3 and 4). A new module (Module VI) in the old group represented the separation of all subcortical regions from the areas known as Modules I and V in the young group. The constitution of the modules in the middle group resembled that in the young group (see Fig. 4). However, the regions in the old group were assembled more densely, leading to the overnumbered regions in modules (see Fig. 4). This finding may indicate that the modular organization of structural brain networks changes greatly until old age. Second, the number of connectors in the old group was also less than that in the young and middle groups (Table IV). The connectors were crucial for the global coordination of information flow in the brain networks and were of great importance for maintaining network integrity [He et al., 2009b; Sporns et al., 2007]. Moreover, the modules in the old group seemed to be more locally organized, resulting in fewer intermodule connections as compared with the numbers in the young and middle group (see Fig. 5). The intermodule connections facilitate communication between different modules and contribute to the network bridges that serve as pivotal connections for the information flow of the whole brain network [Chen et al., 2008; He et al., 2009b]. This finding was in accordance with a previous study on age-related changes in modular organization of human brain functional networks, in which the number of intermodule connections to frontal modular regions was significantly reduced in an old group [Meunier et al., 2009a]. As a result, three connector-modules were identified in both the young and middle groups, whereas no connector-module was found in the old group (Table IV). The connector-module may play a critical role in coordinating activity across the brain network as a whole and in mediating interactions between modules [Meunier et al., 2009a]. Combined with the findings in the small-world properties and node betweenness, these results may reveal that the structural brain network changed slightly, shifting into a more distributed organization during the transition from young to middle age, and then organizing into a localized organization with great alteration in old age. Our findings were also in agreement with a recent study on functional brain networks, which indicated the organization of multiple functional networks shifts from a local anatomical emphasis in children to a more "distributed" organization in young adults over development [Fair et al., 2009].

METHODOLOGY

The human brain structural network was first constructed by using cortical thickness measurements [He et al., 2007], because of strong correlations between regions that are axonally connected [Lerch et al., 2006]. We used the measurement of RGMV to construct structural brain networks, as applied first by a previous study on the hierarchical organization of human cortical networks [Bassett et al., 2008]. Although there is still no direct proof that correlations of gray matter volume across subjects are indicative of axonal connectivity via white matter tracts, strong correlations between brain regions known to be anatomically connected have been observed in previous optimized voxel-based morphometry studies [Mechelli et al., 2005; Pezawas et al., 2005]. Thus, the RGMV as the measurement of structural connectivity is currently considered as exploratory and should be investigated further in future studies. Salvador et al. showed that regional volume had a positive correlation which its mutual information that measured the functional connectivity between the region and the rest brain regions [Salvador et al., 2008]. A previous study also indicates that network properties (e.g., small-worldness and degree distribution) change with the alterations of topological organization introduced by the different parcellation schemes [Wang et al., 2009a]. Thus, the comparison of network parameters across studies must be made with reference to the spatial scale of the parcellation schemes [Zalesky et al., 2010]. While this study was a cross-sectional study, a longitudinal analysis would also be useful to investigate the change in structural brain networks with normal aging. Because all subjects in this study were more than 20 years old, young and adolescent subjects are expected to be included in future studies of brain network development. It is also important to investigate the topological properties and modular organization of human brain networks with normal aging, in combination with functional and structural studies.

CONCLUSION

In this study, we quantitatively analyzed the changes in small-world properties and modularity of structural brain networks with normal aging, using the structural MRI. Our results indicated that normal aging had a notable effect on the topological organization of structural brain networks. These findings were compatible with previous studies on the small-world and modular organization of brain functional and structural networks, thus enhancing our understanding of the underlying physiology of normal aging in the human brain.

ACKNOWLEDGMENTS

The authors are grateful to the anonymous referees for their significant and constructive comments and suggestions, which greatly improved the article. The brain MRI database was constructed at the Aoba Brain Imaging Center with a grant from the Telecommunications Advancement Organization (National Institute of Information and Communications Technology) of Japan. The work in the present study had been partially reported at the 7th International Symposium on Nano-Biomedical Engineering, October 16–17, 2008, National Cheng Kung University, Tainan, Taiwan; and at the 4th Asian Pacific Conference on Biomechanics, April 14–17, 2009, University of Canterbury, Christchurch, New Zealand. The authors thank American Journal Experts (http://www.journalexperts.com/) for English editing and proofreading.

REFERENCES

Achard S, Bullmore E (2007): Efficiency and cost of economical brain functional networks. Plops Comput Biol 3:e17.

Achard S, Salvador R, Whitcher B, Suckling J, Bullmore E (2006): A resilient, low-frequency, small-world human brain functional network with highly connected association cortical hubs. J Neurosci 26:63–72.

Albert M, Knoefel J. 1994. Clinical Neurology of Aging. New York: Oxford University Press.

Bassett DS, Bullmore E (2006): Small-world brain networks. Neuroscientist 12:512–523.

Bassett DS, Meyer-Lindenberg A, Achard S, Duke T, Bullmore E (2006): Adaptive reconfiguration of fractal small-world human brain functional networks. Proc Natl Acad Sci USA 103:19518–19523.

Bassett DS, Bullmore E, Verchinski BA, Mattay VS, Weinberger DR, Meyer-Lindenberg A (2008): Hierarchical organization of human cortical networks in health and schizophrenia. J Neurosci 28:9239–9248.

Bergfield KL, Hanson KD, Chen K, Teipel SJ, Hampel H, Rapoport SI, Moeller JR, Alexander GE (2010): Age-related networks of regional covariance in MRI gray matter: Reproducible multivariate patterns in healthy aging. Neuroimage 49:1750–1759.

Bullmore E, Sporns O (2009): Complex brain networks: Graph theoretical analysis of structural and functional systems. Nat Rev Neurosci 10:186–198.

Bullmore ET, Suckling J, Overmeyer S, Rabe-Hesketh S, Taylor E, Brammer MJ (1999): Global, voxel, and cluster tests, by theory and permutation, for a difference between two groups of structural MR images of the brain. IEEE Trans Med Imaging 18:32–42.

Catani M, ffytche DH (2005): The rises and falls of disconnection syndromes. Brain 128:2224–2239.

Chen ZJ, He Y, Rosa-Neto P, Germann J, Evans AC (2008): Revealing modular architecture of human brain structural networks by using cortical thickness from MRI. Cereb Cortex 18:2374–2381.

Clauset A, Newman MEJ, Moore C (2004): Finding community structure in very large networks. Phys Rev E 70:66111.

Costa LdF, Rodrigues FA, Travieso G, Boas PRV (2007): Characterization of complex networks: A survey of measurements. Adv Phys 56:167–242.

Danon L, Duch J, Diaz-Guilera A, Arenas A (2005): Comparing community structure identification. J Stat Mech 9:P09008.

Eguiluz VM, Chialvo DR, Cecchi GA, Baliki M, Apkarian AV (2005): Scale-free brain functional networks. Phys Rev Lett 94:018102.

Fair DA, Cohen AL, Power JD, Dosenbach NU, Church JA, Miezin FM, Schlaggar BL, Petersen SE (2009): Functional brain networks develop from a "local to distributed" organization. PLoS Comput Biol 5:e1000381.

Ferrarini L, Veer IM, Baerends E, van Tol MJ, Renken RJ, van der Wee NJ, Veltman DJ, Aleman A, Zitman FG, Penninx BW, van Buchem MA, Reiber JH, Rombouts SA, Milles J (2009): Hierarchical functional modularity in the resting-state human brain. Hum Brain Mapp 30:2220–2231.

Ferri R, Rundo F, Bruni O, Terzano MG, Stam CJ (2007). Small-world network organization of functional connectivity of EEG slow-wave activity during sleep. Clin Neurophysiol 118:449–456.

Freeman LC (1977): A set of measures of centrality based on betweenness. Sociometry 40:35–41.

Friston KJ, Holmes AP, Worsley KJ, Poline JP, Frith CD, Frackowiak RSJ (1995): Statistical parametric maps in functional imaging: A general linear approach. Hum Brain Mapp 2:189–210.

Ge Y, Grossman RI, Babb JS, Rabin ML, Mannon LJ, Kolson DL (2002a): Age-related total gray matter and white matter changes in normal adult brain. Part I: volumetric MR imaging analysis. AJNR Am J Neuroradiol 23:1327–1333.

Ge Y, Grossman RI, Babb JS, Rabin ML, Mannon LJ, Kolson DL (2002b): Age-related total gray matter and white matter changes in normal adult brain. Part II: Quantitative magnetization transfer ratio histogram analysis. AJNR Am J Neuroradiol 23:1334–1341.

Genovese CR, Lazar NA, Nichols T (2002): Thresholding of statistical maps in functional neuroimaging using the false discovery rate. Neuroimage 15:870–878.

Girvan M, Newman MEJ (2002): Community structure in social and biological networks. Proc Natl Acad Sci USA 99:7821–7826.

Gong G, Rosa-Neto P, Carbonell F, Chen ZJ, He Y, Evans AC (2009a): Age- and gender-related differences in the cortical anatomical network. J Neurosci 29:15684–15693.

Gong G, He Y, Concha L, Lebel C, Gross DW, Evans AC, Beaulieu C (2009b): Mapping anatomical connectivity patterns of human cerebral cortex using in vivo diffusion tensor imaging tractography. Cereb Cortex 19:524–536.

Guimerà R, Amaral LAN (2005a): Functional cartography of complex metabolic networks. Nature 433:895–900.

Guimerà R, Amaral LAN (2005b): Cartography of complex networks: Modules and universal roles. J Stat Mech 2:P02001.

Guimerà R, Sales-Pardo M, Amaral LAN (2004): Modularity from fluctuations in random graphs and complex networks. Phys Rev E 70:25101.

Guimerà R, Mossa S, Turtschi A, Amaral LAN (2005): The worldwide air transportation network: Anomalous centrality, community structure, and cities' global roles. Proc Natl Acad Sci USA 102:7794–7799.

Hagmann P, Kurant M, Gigandet X, Thiran P, Wedeen VJ, Meuli R, Thiran JP (2007): Mapping human whole-brain structural networks with diffusion MRI. PLoS ONE 2:e597.

Hagmann P, Cammoun L, Gigandet X, Meuli R, Honey CJ, Wedeen VJ, Sporns O (2008): Mapping the structural core of human cerebral cortex. PLoS Biol 6:e159.

Hartwell LH, Hopfield JJ, Leibler S, Murray AW (1999): From molecular to modular cell biology. Nature 402:47–52.

He Y, Chen ZJ, Evans AC (2007): Small-world anatomical networks in the human brain revealed by cortical thickness from MRI. Cereb Cortex 17:2407–2419.

He Y, Chen ZJ, Evans AC (2008): Structural insights into aberrant topological patterns of large-scale cortical networks in Alzheimer's disease. J Neurosci 28:4756–4766.

He Y, Dagher A, Chen Z, Charil A, Zijdenbos A, Worsley K, Evans A (2009a): Impaired small-world efficiency in structural cortical networks in multiple sclerosis associated with white matter lesion load. Brain 132:3366–3379.

He Y, Wang J, Wang L, Chen ZJ, Yan C, Yang H, Tang H, Zhu C, Gong Q, Zang Y, Evans AC (2009b): Uncovering intrinsic modular organization of spontaneous brain activity in humans. PLoS One 4:e5226.

Hedden T, Gabrieli JDE (2004): Insights into the ageing mind: A view from cognitive neuroscience. Nat Rev Neurosci 5:87–96.

Iturria-Medina Y, Sotero RC, Canales-Rodriguez EJ, Aleman-Gomez Y, Melie-Garcia L (2008): Studying the human brain anatomical network via diffusion-weighted MRI and graph theory. Neuroimage 40:1064–1076.

Jean Talairach PT. 1988. Co-Planar Stereotaxic Atlas of the Human Brain. Stuttgart: Thieme.

Kamada T, Kawai S (1989): An algorithm for drawing general undirected graphs. Inform Process Lett 31:7–15.

Kashtan N, Alon U (2005): Spontaneous evolution of modularity and network motifs. Proc Natl Acad Sci USA 102:13773–13778.

Lancaster JL, Woldorff MG, Parsons LM, Liotti M, Freitas CS, Rainey L, Kochunov PV, Nickerson D, Mikiten SA, Fox PT (2000): Automated Talairach atlas labels for functional brain mapping. Hum Brain Mapp 10:120–131.

Latora V, Marchiori M (2001): Efficient behavior of small-world networks. Phys Rev Lett 87:198701.

Lerch JP, Worsley K, Shaw WP, Greenstein DK, Lenroot RK, Giedd J, Evans AC (2006): Mapping anatomical correlations across cerebral cortex (MACACC) using cortical thickness from MRI. Neuroimage 31:993–1003.

Li Y, Liu Y, Li J, Qin W, Li K, Yu C, Jiang T (2009): Brain anatomical network and intelligence. PLoS Comput Biol 5:e1000395.

Liu Y, Liang M, Zhou Y, He Y, Hao Y, Song M, Yu C, Liu H, Liu Z, Jiang T (2008): Disrupted small-world networks in schizophrenia. Brain 131:945–961.

Maldjian JA, Laurienti PJ, Kraft RA, Burdette JH (2003): An automated method for neuroanatomic and cytoarchitectonic atlas-based interrogation of fMRI data sets. Neuroimage 19:1233–1239.

Maldjian JA, Laurienti PJ, Burdette JH (2004): Precentral gyrus discrepancy in electronic versions of the Talairach atlas. Neuroimage 21:450–455.

Mechelli A, Friston KJ, Frackowiak RS, Price CJ (2005): Structural covariance in the human cortex. J Neurosci 25:8303–8310.

Mesulam MM (1998): From sensation to cognition. Brain 121:1013–1052.

Meunier D, Achard S, Morcom A, Bullmore E (2009a): Age-related changes in modular organization of human brain functional networks. Neuroimage 44:715–723.

Meunier D, Lambiotte R, Fornito A, Ersche KD, Bullmore ET (2009b): Hierarchical modularity in human brain functional networks. Front Neuroinformatics 3:37.

Micheloyannis S, Pachou E, Stam CJ, Vourkas M, Erimaki S, Tsirka V (2006): Using graph theoretical analysis of multi channel EEG to evaluate the neural efficiency hypothesis. Neurosci Lett 402:273–277.

Micheloyannis S, Vourkas M, Tsirka V, Karakonstantaki E, Kanatsouli K, Stam CJ (2009): The influence of ageing on complex brain networks: A graph theoretical analysis. Hum Brain Mapp 30:200–208.

Newman MEJ (2004): Fast algorithm for detecting community structure in networks. Phys Rev E 69:066133.

Newman MEJ (2006a): Modularity and community structure in networks. Proc Natl Acad Sci USA 103:8577–8582.

Newman MEJ (2006b): Finding community structure in networks using the eigenvectors of matrices. Phys Rev E 74:36104.

Newman MEJ, Girvan M (2004): Finding and evaluating community structure in networks. Phys Rev E 69:026113.

Pezawas L, Meyer-Lindenberg A, Drabant EM, Verchinski BA, Munoz KE, Kolachana BS, Egan MF, Mattay VS, Hariri AR, Weinberger DR (2005): 5-HTTLPR polymorphism impacts human cingulate-amygdala interactions: A genetic susceptibility mechanism for depression. Nat Neurosci 8:828–834.

Radicchi F, Castellano C, Cecconi F, Loreto V, Parisi D (2004): Defining and identifying communities in networks. Proc Natl Acad Sci USA 101:2658–2663.

Redies C, Puelles L (2001): Modularity in vertebrate brain development and evolution. Bioessays 23:1100–1011.

Reichardt J, Bornholdt S (2006): When are networks truly modular? Phys D 224:20–26.

Resnick SM, Pham DL, Kraut MA, Zonderman AB, Davatzikos C (2003): Longitudinal magnetic resonance imaging studies of older adults: a shrinking brain. J Neurosci 23:3295–3301.

Robinson PA, Henderson JA, Matar E, Riley P, Gray RT (2009): Dynamical reconnection and stability constraints on cortical network architecture. Phys Rev Lett 103:108104.

Salvador R, Suckling J, Coleman MR, Pickard JD, Menon D, Bullmore E (2005): Neurophysiological architecture of functional magnetic resonance images of human brain. Cereb Cortex 15:1332–1342.

Salvador R, Martiez A, Pomarol-Clotet E, Gomar J, Vila F, Sarró S, Capdevila A, Bullmore E (2008): A simple view of the brain through a frequency-specific functional connectivity measure. NeuroImage 39:279–289.

Sato K, Taki Y, Fukuda H, Kawashima R (2003): Neuroanatomical database of normal Japanese brains. Neural Netw 16:1301–1310.

Smith CD, Chebrolu H, Wekstein DR, Schmitt FA, Markesbery WR (2007): Age and gender effects on human brain anatomy: A voxel-based morphometric study in healthy elderly. Neurobiol Aging 28:1075–1087.

Sowell ER, Peterson BS, Thompson PM, Welcome SE, Henkenius AL, Toga AW (2003): Mapping cortical change across the human life span. Nat Neurosci 6:309–315.

Sowell ER, Thompson PM, Leonard CM, Welcome SE, Kan E, Toga AW (2004): Longitudinal mapping of cortical thickness and brain growth in normal children. J Neurosci 24:8223–8231.

Sporns O, Zwi J (2004): The small world of the cerebral cortex. Neuroinformatics 2:145–162.

Sporns O, Tononi G, Edelman GM (2000): Theoretical neuroanatomy: Relating anatomical and functional connectivity in graphs and cortical connection matrices. Cereb Cortex 10:127–141.

Sporns O, Honey CJ, Kotter R (2007): Identification and classification of hubs in brain networks. PLoS ONE 2:e1049.

Stam CJ, Jones BF, Nolte G, Breakspear M, Scheltens P (2007): Small-world networks and functional connectivity in Alzheimer's disease. Cereb Cortex 17:92–99.

Strogatz SH (2001): Exploring complex networks. Nature 410:268–276.

Supekar K, Musen M, Menon V (2009): Development of large-scale functional brain networks in children. PLoS Biol 7:e1000157.

Taki Y, Kinomura S, Sato K, Goto R, Kawashima R, Fukuda H (2009): A longitudinal study of gray matter volume decline with age and modifying factors. Neurobiol Aging: doi:10.1016/j.neurobiolaging.2009.05.003.

Tisserand DJ, van Boxtel MPJ, Pruessner JC, Hofman P, Evans AC, Jolles J (2004): A voxel-based morphometric study to determine individual differences in gray matter density associated with age and cognitive change over time. Cereb Cortex 14:966–973.

Tzourio-Mazoyer N, Landeau B, Papathanassiou D, Crivello F, Etard O, Delcroix N, Mazoyer B, Joliot M (2002): Automated anatomical labeling of activations in SPM using a macroscopic anatomical parcellation of the MNI MRI single-subject brain. Neuroimage 15:273–289.

Valencia M, Pastor MA, Fernández-Seara MA, Artieda J, Martinerie J, Chavez M (2009): Complex modular structure of large-scale brain networks. Chaos 19:023119.

van den Heuvel MP, Stam CJ, Kahn RS, Hulshoff Pol HE (2009): Efficiency of functional brain networks and intellectual performance. J Neurosci 29:7619–7624.

Van Essen DC (2005): A population-average, landmark- and surface-based (PALS) atlas of human cerebral cortex. NeuroImage 28:635–662.

Wang J, Wang L, Zang Y, Yang H, Tang H, Gong Q, Chen Z, Zhu C, He Y (2009a): Parcellation-dependent small-world brain functional networks: A resting-state fMRI study. Hum Brain Mapp 30:1511–1523.

Wang L, Zhu C, He Y, Zang Y, Cao Q, Zhang H, Zhong Q, Wang Y (2009b): Altered small-world brain functional networks in children with attention-deficit/hyperactivity disorder. Hum Brain Mapp 30:638–649.

Watts DJ, Strogatz SH (1998): Collective dynamics of "small-world" networks. Nature 393:440–442.

Zalesky A, Fornito A, Harding IH, Cocchi L, Yücel M, Pantelis C, Bullmore ET (2010): Whole-brain anatomical networks: Does the choice of nodes matter? NeuroImage 50:970–983.

Cardiovascular Engineering and Technology, Vol. 3, No. 1, March 2012 (© 2011) pp. 41–51
DOI: 10.1007/s13239-011-0067-1

Evaluation of Rupture Properties of Thoracic Aortic Aneurysms in a Pressure-Imposed Test for Rupture Risk Estimation

SHUKEI SUGITA,[1,3] TAKEO MATSUMOTO,[1,4] TOSHIRO OHASHI,[1] KIICHIRO KUMAGAI,[2] HIROJI AKIMOTO,[2] KOICHI TABAYASHI,[2] and MASAAKI SATO[1]

[1]Department of Mechatronics and Precision Engineering, Graduate School of Engineering, Tohoku University, 6-6-01 Aramaki Aza Aoba, Aoba-ku, Sendai 980-8579, Japan; [2]Department of Cardiovascular Surgery, Graduate School of Medicine, Tohoku University, 2-1 Seiryo-machi, Aoba-ku, Sendai 980-8574, Japan; [3]Center for Fostering Young and Innovative Researchers, Nagoya Institute of Technology, Gokiso-cho, Showa-ku, Nagoya 466-8555, Japan; and [4]Biomechanics Laboratory, Department of Mechanical Engineering, Nagoya Institute of Technology, Gokiso-cho, Showa-ku, Nagoya 466-8555, Japan

(Received 24 July 2011; accepted 7 October 2011; published online 27 October 2011)

Associate Editor Tim McGloughlin oversaw the review of this article.

Abstract—Rupture properties of thoracic aortic aneurysms (TAAs) were measured *in vitro* in a pressure-imposed test to predict the ultimate stress of TAAs from their mechanical behavior in a physiological pressure range. Each quadrilateral (ca. 20 × 20 mm^2) specimen of TAAs or porcine thoracic aortas (PTAs) was pressurized from the inner wall until rupture or up to 4500 mmHg, while its deformation was being monitored. In-plane stress σ and strain ε of the specimen were calculated using Laplace's law and deformations of the markers drawn on the specimen surface, respectively. Ultimate stress σ_{max} and tangent elastic modulus H were determined from the σ–ε curve as its maximum stress and slope, respectively. The tangent elastic modulus H of PTA specimens tended to increase with the increase in σ, while that of TAA specimens tended to reach a plateau in a low-σ region. This tendency was confirmed by fitting a function $H = C_\sigma(1 - \exp(-\sigma/\tau_\sigma))$ to the H–σ relation of specimens: The yielding parameter τ_σ was significantly lower in TAAs than PTAs. Furthermore, the logarithm of the parameter τ_σ correlated significantly with σ_{max}, for all specimens. These results may indicate that τ_σ is one of the candidate indices for rupture risk estimation.

Keywords—Thoracic aortic aneurysm, Pressure-imposed test, Mechanical property, Rupture estimation, Tangent elastic modulus.

INTRODUCTION

The number of deaths caused by rupture of all aortic aneurysms has been increasing. For example, in Japan these deaths were recorded as 8.3, 8.6, and 9.3–100,000 people in 2006, 2007, and 2008, respectively,[20,21] possibly because of the rapid aging in this country. While only about 30% of aortic aneurysms result in rupture,[18,19], the mortality rate due to the rupture of thoracic aneurysms has been reported to be more than 90%.[8] At present, aneurysms with a diameter larger than a critical value, ca. 5 cm for example, are surgically repaired. However, one of the problems is that aneurysms with smaller diameters than the critical value could rupture.[1,3,4] Therefore, other reliable indices that can be used to estimate the risk of aneurysmal rupture have been urgently required.

From the viewpoint of the strength of materials, aneurysms rupture when the tensile stress in the wall exceeds its ultimate stress. Therefore, many studies have reported the mechanical properties of aneurysms. Stress distribution in an aneurysmal wall has been estimated based on patient-specific mathematical models constructed from CT images.[5,9,15] The mechanical properties of aortic aneurysms have been measured with uniaxial[14,16] tensile tests *in vitro*, and it has been reported that their ultimate stress was lower than that of normal aortas, while aneurysm specimens were much stiffer than the normal ones. Although there has been a wealth of data on the mechanical properties of aneurysms, these data are not sufficient for a reliable risk estimation of aneurysm rupture in each patient because there is a wide variety of data. We need to develop a patient-specific method to estimate the ultimate stress from clinical data such as beat-by-beat deformation of the aneurysm.

Address correspondence to Takeo Matsumoto, Biomechanics Laboratory, Department of Mechanical Engineering, Nagoya Institute of Technology, Gokiso-cho, Showa-ku, Nagoya 466-8555, Japan. Electronic mail: takeo@nitech.ac.jp

1869-408X/12/0300-0041/0

Since aneurysmal tissues are biaxially stretched *in vivo*, mechanical properties should be evaluated in a biaxial tensile test. Although elastic moduli of aneurysmal specimens have been obtained in biaxial tensile tests,[6,11,14] ultimate stress has not been acquired due to technical difficulties in chucking specimens until failure. To mimic the mechanical environment in situ more rigorously, Groenink *et al.*[7] reported a pressure-imposed test for a whole segment of normal human thoracic aortas. An application of this method to real aneurysms would be unrealistic due to difficulties in obtaining whole segments of aneurysms during surgery. To solve this problem, we previously developed a pressure-imposed rupture test system for small quadrilateral segments and successfully obtained mechanical properties of porcine thoracic aortas (PTAs) including the failure strength, as we accomplished in the conventional uniaxial tensile test.[13]

In this study, we applied this system to specimens obtained from unruptured human thoracic aortic aneurysms (TAAs) to measure their ultimate stress σ_{max} and other mechanical properties that would be measurable in clinical MRI and CT data, such as the local strain and tangent elastic modulus. We then searched for significant correlations between σ_{max} and other mechanical parameters to estimate the ultimate stress with clinically measurable parameters, and found that the shape of a tangent elastic modulus–intramural stress relationship had a significant correlation with the ultimate stress.

MATERIALS AND METHODS

Specimens

Quadrilateral TAA specimens were obtained from patients following their informed consent during aortic replacement surgery in Tohoku University Hospital with the approval of the Tohoku University Hospital Human Studies Committee according to the World Medical Association Declaration of Helsinki. The TAA specimens were immersed in a physiological saline and stored frozen at −20 °C until experiments for 8 months at the longest since mechanical properties of aortas after freezing have been reported to be comparable to those before freezing.[17] About half of the specimens were unsuitable for the pressure-imposed test because they were too small to mount on the tester. The remaining 15 specimens from 12 patients (11 males and 1 female; age: 69 ± 8) were used for the pressure-imposed test. Data concerning patients and specimens are listed in Table 1.

As control, PTAs were obtained at a local slaughterhouse. Quadrilateral specimens (ca. 20 mm × 20 mm) were excised near the first (proximal) and fifth or sixth (distal) intercostal arteries. The PTAs were immersed in physiological saline (154 mM NaCl) and kept at −20 °C until experiments in a manner similar to the TAA specimens.

TABLE 1. Summary of the origin, sex, age, position, and dimensions of aneurysm specimens.

Specimen #	Origin[a]	Sex	Age	Position	Diameter (mm)	Thickness (mm)
H0104A	AAE	Female	74	Descending	50	2.7
H0104B						2.5
H0108	TA	Male	68	Arch	50	3.3
H0109	AD	Male	70	Descending	62	3.4
H0110	TA	Male	82	Descending	57	2.4
H0112	–	Male	59	Arch	75	3.1
H0113A	AD	Male	74	Ascending	50	3.4
H0113B						5.6
H0115	TA	Male	68	Descending	65	2.8
H0116A	TA	Male	73	Arch	65	3.8
H0117	TA	Male	76	Arch	70	5.0
H0119A	TA	Male	67	Arch	62	4.3
H0122A	AD	Male	51	Descending	75	3.3
H0122B						3.5
H0123	TA	Male	63	Descending	65	4.1
Mean ± SD			69 ± 8		62 ± 9	3.5 ± 0.9

AAE, annulo aortic ectasia; TA, true aneurysm; AD, aortic dissection. Since specimens with the same number (e.g. H0104A and H0104B) were obtained from the same aneurysm of the same patient, data except thickness are common. Mean ± SD for age and diameter was calculated for the number of patients.

Pressure-Imposed Test

The pressure-imposed test was performed as described previously.[13] Briefly, the thickness of each specimen was measured five times at different places with an area micrometer by sandwiching the specimen with glass plates to avoid squeezing the tip of the micrometer into the specimens,[12] and the data were averaged to obtain specimen thickness at the no-load state. A dot matrix at 2-mm intervals in circumferential and longitudinal directions was marked on the adventitial surface of the specimen with black Indian ink. The specimen was then fixed on the pressure-imposed test system. Figure 1 shows a schematic illustration of the experimental setup of the system. After the circumferential direction of the specimen was oriented horizontally referring to suture knots tied during surgery, the specimen was sandwiched with a metal block and a plate both having a hole 15 mm in diameter, and fixed with bolts. Air pressure generated from the compressor was controlled with an electro-pneumatic regulator and applied to the specimen through a rubber balloon through the hole of the metal block to make the specimen bulge into the hole of the metal plate. The method of loading pressure through the rubber balloon was chosen to avoid air leaks. To avoid generation of membrane tension of the rubber balloon, a relatively large balloon was used and it was confirmed that the balloon had wrinkles, i.e., it did not bear tension even at the rupture of the specimens. The balloon was pressurized at a rate of 10 mmHg/s until the specimen was ruptured or its pressure reached 4500 mmHg. The electro-pneumatic regulator was controlled with data acquisition software (LabVIEW 5.0, National Instruments, Japan) on a personal computer (PC) through a digital-analog converter. The actual pressure loaded onto the specimen was measured with a pressure transducer, and then recorded on the PC through a strain amplifier and an analog–digital converter at a sampling rate of 100 kHz. Images of deformation of the specimens were captured with charged coupled device (CCD) video cameras (resolution: ~11 pixel/mm) placed at both front and lateral sides of the specimen and recorded by a video cassette recorder through a digital video mixer. Images of the specimens at rupture were also acquired with a high-speed camera (FIRSTCAM-Net 1000/Max, Photron, Japan; resolution: ~27 pixel/mm) at 3000 frames/s to identify the point of crack initiation.

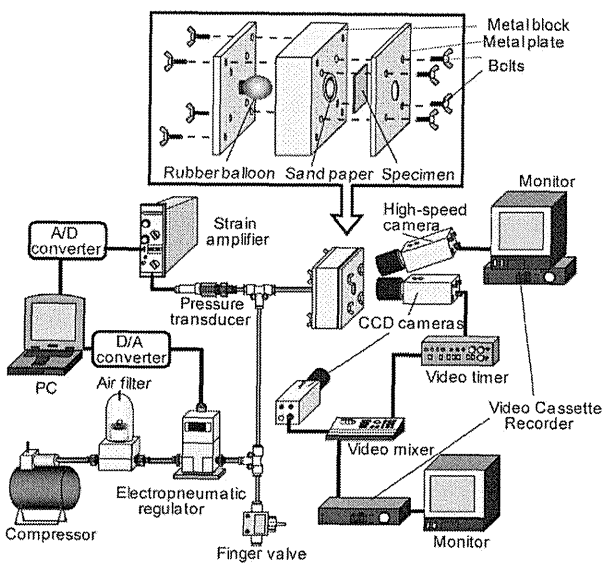

FIGURE 1. Schematic illustration of the experimental setup.

The specimens were then removed from the apparatus following the test, and crack shapes of the ruptured specimens were manually traced on both adventitial and intimal sides. The angle between the major axis of an equivalent ellipse of the crack shape and the circumferential direction of the specimen *in vivo* was then measured as a crack direction with image analysis software (ImageJ 1.42i, National Institutes of Health, Bethesda, MD, USA).

Mechanical Parameters

The in-plane stress and strain of each specimen during pressurization were calculated every 10 mmHg from the specimen geometries and the applied pressure, assuming that the specimen was incompressible and had a thin-walled shape with uniform thickness. The idealized geometry used for the calculation is shown in Fig. 2. The shape of the specimen was assumed to be a circular plate at the no-load state (Fig. 2a), an oblate spheroid when the maximum deformation D_{max} was less than the radius of the hole of the metal plate r ($D_{max} < r = 7.5$ mm; Fig. 2b), and a combined geometry comprising a hemisphere and a cylinder when $D_{max} \geq r$ (Fig. 2c). The maximum deformation D_{max} was determined as the maximum displacement of the specimen in the direction perpendicular to the plane of the specimen at the no-load condition. This geometrical approximation was found to be reasonable by comparing the mathematical curve with the shape of the specimen during pressurization.[13]

Based on the geometrical approximation and incompressibility of the specimens, the in-plane stress σ was obtained as follows (see Appendices A and B in Online Resource):

$$\sigma = \frac{P}{2tD_{max}}\left\{r^2 + \frac{D_{max}^2}{e}\log\left[\frac{r(e+1)}{D_{max}}\right]\right\}, \quad e = \frac{\sqrt{D_{max}^2 - r^2}}{r} \quad (D_{max} < r) \tag{1}$$

$$\sigma = \frac{PD_{max}}{t}, \quad (D_{max} \geq r) \tag{2}$$

where P is pressure, t is the wall thickness at the no-load state, and e the eccentricity of an oblate spheroid (see Appendix C in Online Resource). The ultimate stress σ_{max} was then determined as its maximum stress during pressurization.

The in-plane strain ε of each specimen was calculated from changes in the dimensions of the specimen surface as follows (see Appendix D in Online Resource):

$$\varepsilon \approx \frac{\pi(r + D_{max})}{4r}\left[1 + \frac{1}{4}\left(\frac{r - D_{max}}{r + D_{max}}\right)^2 + \frac{1}{64}\left(\frac{r - D_{max}}{r + D_{max}}\right)^4 + \frac{1}{256}\left(\frac{r - D_{max}}{r + D_{max}}\right)^6\right] - 1 \quad (D_{max} < r) \tag{3}$$

$$\varepsilon = \frac{\pi r + 2(D_{max} - r)}{2r} - 1. \quad (D_{max} \geq r) \tag{4}$$

The tangent elastic modulus H was then calculated from the stress–strain curve of each specimen as the increment in the stress divided by the increase in the mean strain during the pressurization, as shown by the following equation:

$$H = \frac{\Delta\sigma}{\Delta\varepsilon}. \tag{5}$$

The moving average was then performed twice (triangular moving average) for three data points for smoothing. The maximum tangent elastic modulus H_{max} was determined as the maximum value of H during pressurization.

Local deformations of the specimens were measured from the changes in the distances between the dots marked on the specimen's surface. Firstly, space coordinates of each of the 4 × 4 dots marked on the specimen surface were determined. Both x and y coordinates were obtained from the images captured from the front CCD camera. Z coordinates were determined from the measured D_{max} in images acquired

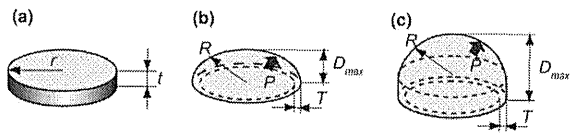

FIGURE 2. Idealized shapes of specimens assumed for the analysis. Each specimen is regarded initially as a circular plate set on the pressure-imposed test system (a), an oblate spheroid until $D_{max} < r$ (b), and a combined geometry comprising a hemisphere and a cylinder for $D_{max} \geq r$ (c). *r*, radius of the hole of the metal plate; *t*, thickness at the no-load state; *R*, curvature radius of the specimen; *P*, pressure; *T*, thickness of the specimen; D_{max}, the maximum deformation of the specimen.

from the lateral CCD camera assuming the dots were on an idealized specimen surface (Appendix E in Online Resource). After distances between two adjacent dots were measured in the 3D coordinates, local stretch ratios in both circumferential (λ_{circ}) and longitudinal (λ_{long}) directions were calculated relative to the distance at no-load conditions. Then, for each quadrilateral area surrounded by four dots, neighboring local stretch ratios were averaged in each direction $\overline{\lambda_{circ}}$ and $\overline{\lambda_{long}}$, and finally the local area strain ε_{area} was calculated as follows:

$$\varepsilon_{area} = \overline{\lambda_{circ}} \cdot \overline{\lambda_{long}} - 1. \quad (6)$$

The rupture site was determined as the site where a crack initiated on the adventitial surface as observed with the high-speed camera. To evaluate the heterogeneity of the specimens, the variance of the local area strain was calculated as the ratio of the local area strain to its averaged value in each specimen.

Statistical Analysis

Data are expressed as mean ± standard deviation (SD). Differences between two groups were analyzed using Mann–Whitney U test. Differences of data among more than two specimen groups were analyzed by the one-way ANOVA followed by the Bonferroni test for equal variances (σ_{max} and H_{max}), and by the Kruskal–Wallis test followed by the Steel–Dwass test for unequal variances (τ_σ). The F-test was used for analysis of the difference in standard deviation of distributions. Associations between mechanical parameters were assessed using Pearson's correlation coefficient. All hypothesis tests were performed using a significance level of $p = 0.05$.

RESULTS

Eleven of 15 TAA specimens resulted in a successful rupture. Four of the remaining TAA specimens did not rupture even at 4500 mmHg (unruptured TAAs). Six of the 11 ruptured specimens ruptured near the center of the specimen (TAAs ruptured at the center), while the remaining TAA specimens ruptured along the edge of the specimen holder, i.e., the metal plate (TAAs ruptured at the edge). TAAs ruptured at the center and those ruptured at the edge were analyzed separately because the tensile strength calculated for TAAs ruptured at the edge might be smaller than the true tensile strength of the specimens. All PTA specimens ruptured successfully at the center.

Example images of successfully ruptured TAA and PTA specimens after the pressure-imposed test are shown in Fig. 3. For PTA specimens, all the cracks ran mostly in the circumferential direction (Figs. 3c–3e). In contrast, the cracks ran in various directions in TAA specimens (Figs. 3a, 3b, and 3e). Quantitative analysis showed that the deviation of the crack angle on the adventitial surface from the circumferential direction was significantly higher in TAA specimens (55 ± 34°) than PTA specimens (8 ± 7°).

Crack angle on the adventitial side had a poor correlation with that on the intimal side in TAA specimens, while the angles were coherent between both sides in PTA specimens. The difference in the crack angles between the adventitial and intimal sides tended to be higher in TAAs than PTAs ($p = 0.09$, Fig. 3f). This result may indicate that the weakest direction of the wall was almost uniform along the wall thickness for PTAs, but not for TAAs. Furthermore, sequential images acquired with the high-speed camera

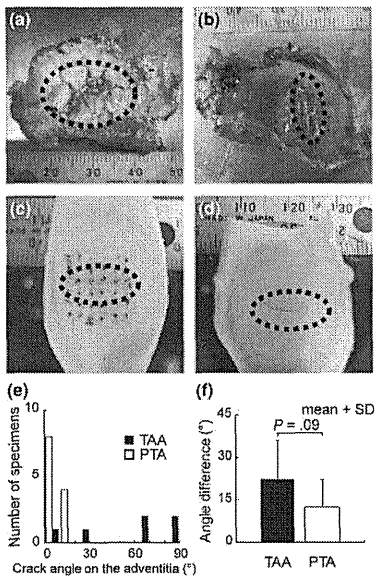

FIGURE 3. Rupture cracks formed after the pressure-imposed test. (a–d) Images of specimens captured from the adventitial (a, c) and intimal (b, d) sides of a TAA (a, b) and a distal PTA (c, d) specimen. Horizontal and upper directions in the images correspond to the circumferential and proximal directions, respectively. (e) Distribution of the crack direction on the adventitial side with the circumferential direction taken as 0°. (f) Difference in crack angle between intimal and adventitial sides.

showed that not only the weakest direction, but also the weakest point of the wall seemed to differ with the wall thickness in some TAAs (Fig. 4, and Movies 1 and 2 in Online Resource). For example, in the specimen shown in Fig. 4a, destruction seemed to happen from the intimal side (Figs. 4b and 4c). After no special phenomena were observed for a few seconds (Fig. 4d), a crack initiated (Fig. 4e) and propagated (Fig. 4f) on the adventitial surface. The crack on the adventitial surface was initiated at a position that differed from that where the destruction was observed on the intimal side. For all PTA specimens (Fig. 4g), the crack was initiated from the adventitial side (Fig. 4h) and propagated in the wall to the intimal side almost at the same point (Fig. 4i).

The local area strain ε_{area} at the rupture site of TAAs ruptured at the center was 135 ± 28% of the average value in each specimen, whereas the maximum value of ε_{area} in each specimen was higher (174 ± 24%). A similar result was obtained for the PTA specimens (rupture site: 110 ± 26% of the average value; maximum value: 144 ± 19%). These observations indicate that the rupture cracks did not always initiate at the point where the highest local area strain ε_{area} was found. The ratio of ε_{area} to its averaged value in each specimen showed a wider distribution in TAAs ruptured at the center (Fig. 5a) than in PTAs (Fig. 5b). The F-test showed that the standard deviation of the distribution of ε_{area} was significantly higher in TAA specimens (0.46) than PTA specimens (0.25), indicating

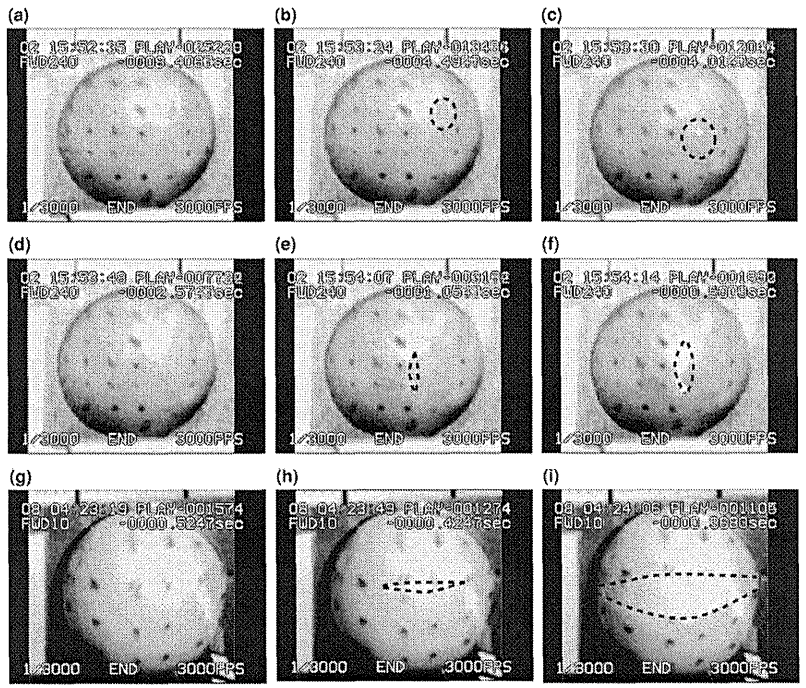

FIGURE 4. Sequential images of rupturing specimens acquired with a digital high-speed camera. (a–f) Images of TAA specimens captured at 0.00 s (a), 3.91 s (b), 4.39 s (c), 5.83 s (d), 7.35 s (e), and 7.90 s (f). (g–i) Images of distal PTA specimens captured at 0.00 s (d), 0.10 s (e), and 0.16 s (f). Areas surrounded by broken curves indicate areas where a micro-rupture seems to have occurred.

that the local area strain was more heterogeneous in TAAs.

The mechanical properties σ_{max} and H_{max} of ruptured TAA and PTA specimens, along with data of unruptured specimens and specimens ruptured at the edge of the specimen holder, are summarized in Table 2. The ultimate stress of TAAs ruptured at the center was significantly lower than that of the distal PTAs. The range of ultimate stresses of both TAAs and PTAs was wide (0.38–1.38 MPa for ruptured TAAs, 1.06–1.88 MPa for unruptured TAAs, and 1.26–3.08 MPa for PTAs), indicating that there were especially weak specimens in the TAAs tested.

Stress–strain relationships of TAAs and PTAs are shown in Figs. 6a and 6b, respectively. Both stress–strain relationships show the non-linear properties of the materials, and the curves of TAA specimens shifted to the left compared to those of PTA, as reported previously.[14,16] The shift was especially remarkable for unruptured TAAs. The relationships between H and σ for TAAs and PTAs are shown in Figs. 6c and 6d, respectively. The parameter H seemed to increase almost monotonically in PTAs with the increase in σ, while it did not increase monotonically and reached a plateau at a relatively lower pressure in ruptured TAAs. To confirm this tendency, H–σ curves were fitted with an exponential function as follows:

$$H = C_\sigma\{1 - e^{-\frac{\sigma}{\tau_\sigma}}\}, \quad (7)$$

where C_σ is the asymptotic value of the tangent elastic modulus, and τ_σ is the value of σ when a tangent line of the fitting function at the origin achieved C_σ (Fig. 7a). The parameter τ_σ is thus an index of stress at which the curve reaches a plateau, i.e., the wall material yields to stress, and is called a yielding parameter. Figure 7b shows the yielding parameter τ_σ in each group. The parameter τ_σ was significantly lower in TAA specimens ruptured at the center and the edge, than in PTA specimens. The tendency for the tangent elastic modulus of ruptured TAA specimens to reach a plateau at a smaller stress was confirmed.

Finally, the correlation between the ultimate stress and other mechanical parameters was analyzed. Figure 8 shows correlations between σ_{max} and H_{max}, and σ_{max} and the natural logarithm of τ_σ. Although the correlations were not significant for TAAs ruptured at the center ($R^2 = 0.64$ and $p = 0.055$ for σ_{max}–H_{max}, $R^2 = 0.40$ and $p = 0.17$ for σ_{max}–τ_σ), they were significant for all ruptured TAAs ($R^2 = 0.40$ and $p < 0.05$ for σ_{max}–H_{max}, $R^2 = 0.48$ and $p < 0.05$ for σ_{max}–τ_σ).

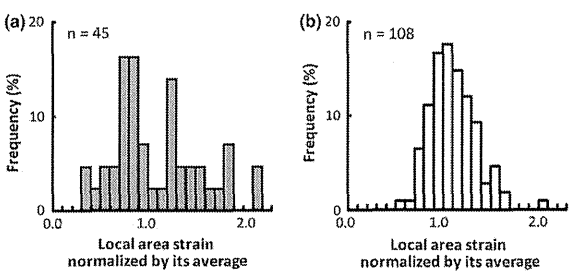

FIGURE 5. Distributions of normalized area strain in TAA (a) and PTA (b) specimens.

TABLE 2. Summary of the mechanical properties measured by the pressure-imposed test.

Specimen	n	σ_{max} (MPa)	H_{max} (MPa)
TAA ruptured at the center	6	0.98 ± 0.39*	4.9 ± 2.5**
TAA ruptured at the edge of the specimen holder	5	(1.02 ± 0.55)[a]	(7.0 ± 3.6)[a]
Unruptured TAA	4	1.56 ± 0.34	13.0 ± 3.6
Proximal PTA	6	1.81 ± 0.43	8.5 ± 5.4
Distal PTA	6	2.29 ± 0.74	9.7 ± 3.9

σ_{max}, ultimate stress; H_{max}, maximum of the incremental elastic modulus. σ_{max} data of the unruptured TAA specimen indicate the maximum value of stress during the pressure-imposed test.
[a]Real value might be higher than this because samples might have been damaged by the edge of the specimen holder.
* $p < 0.05$ vs. distal PTA; ** $p < 0.05$ vs. unruptured TAA.

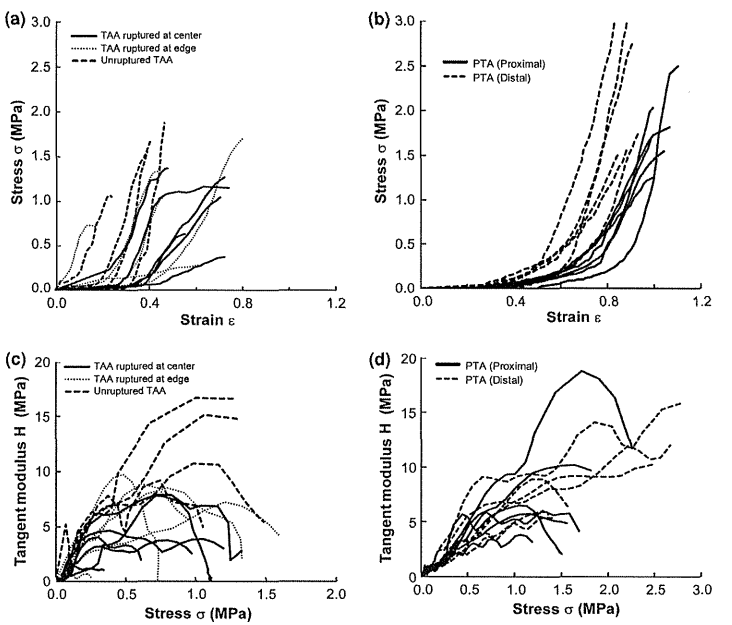

FIGURE 6. Stress–strain curves of TAA (a) and PTA (b) specimens, and tangential modulus–stress curves of TAA (c) and PTA (d) specimens obtained in the pressure-imposed test.

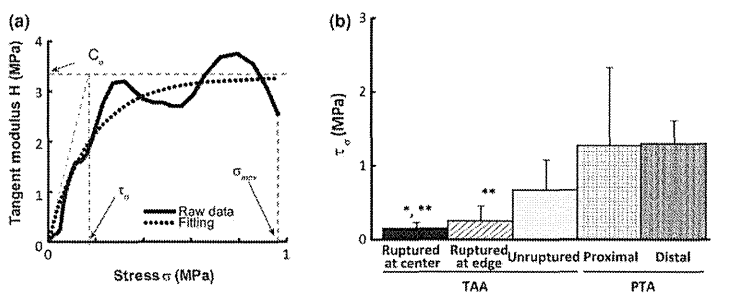

FIGURE 7. Typical tangent modulus–stress curve and its fitting function $H = C_\sigma(1 - \exp(-\sigma/\tau_\sigma))$ to the H–σ relation (a) and parameter τ_σ of TAA and PTA specimens (b). *$p < 0.05$ vs. proximal PTA, **$p < 0.05$ vs. distal PTA.

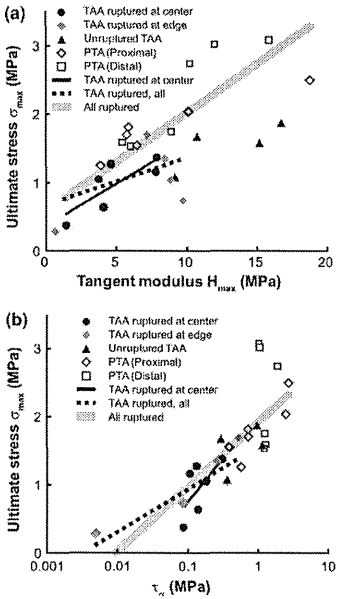

FIGURE 8. Relationships between the ultimate stress σ_{max} and the maximal tangent modulus H_{max} (a), and the ultimate stress and the yielding parameter τ_σ (b). Data obtained from unruptured TAAs are plotted for comparison. The regression lines are obtained from specimens of TAA ruptured at the center (thin lines), TAA ruptured at the center and the edge (broken lines), and all ruptured TAA and PTA specimens (thick lines).

Furthermore, strong correlations were found if PTA specimens were included in the analysis ($R^2 = 0.55$ and $p < 0.0001$ for σ_{max}–H_{max}, $R^2 = 0.51$ and $p < 0.0001$ for σ_{max}–τ_σ).

DISCUSSION

This study performed a pressure-imposed test on TAA and PTA specimens and analyzed the relationship between their ultimate stress and other mechanical parameters to estimate the rupture risk of TAAs based on clinical data. The major findings of this study include verification that (1) the pressure-imposed test was useful to obtain the rupture property of aneurysms, (2) the mechanical property of TAAs was heterogeneous, and finally, but most importantly, (3) the ultimate stress could be estimated from the shape of a tangent elastic modulus–intramural stress relationship.

Usefulness of the Pressure-Imposed Test

The pressure-imposed test showed that the normal aorta was weakest in the longitudinal direction. A similar result was obtained when using the tensile test.[13] In contrast, there was no consistent direction with minimal strength in aneurysmal tissues (Fig. 3e). A study with the tensile test also showed that the directional difference in the ultimate stress between the longitudinal and circumferential directions disappeared in aneurysmal tissues.[16] Furthermore, the crack direction of aneurysmal specimens changed even within a specimen, and the crack angle was not constant, indicating difficulty in determining the weakest direction of aneurysm specimens. If the ultimate stress of a specimen is obtained in a conventional uniaxial tensile test, the strength is of the tensile direction and does not necessarily mean the lowest value among all directions. Thus, the pressure-imposed test is useful for a study of rupture properties because the minimal ultimate stress and its direction can be obtained simultaneously without knowing the weakest direction of specimens before testing.

Mechanical Heterogeneity of TAAs

The distribution of the local area strain was wider in TAA specimens than PTA specimens (Fig. 5), indicating the existence of mechanical heterogeneity in TAA specimens. The observation that the crack direction in TAA specimens differed between intimal and adventitial sides (Figs. 3a–3d and 3f) also showed the heterogeneity in each TAA. If the mechanical properties were homogeneous within the wall, the crack should propagate from one side to the other at almost the same point as in PTA specimens. Furthermore, some cracks in TAA specimens propagated from their intimal side, whereas those in all PTA specimens propagated from their adventitial side (Fig. 4), indicating that heterogeneity exists even in the thickness direction.

Feasibility for Estimation of Ultimate Stress

The purpose of this study was to establish a method to predict the ultimate stress of TAAs. In the beginning, we speculated that a higher local strain might correlate with the rupturing site. However, the rupture cracks did not always initiate at the point with the highest local area strain, indicating the difficulty of

predicting rupture when only using local area strain data. Thus, we investigated the correlation between various mechanical parameters to estimate the ultimate stress from other mechanical parameters. Firstly, a significant correlation was found between the ultimate stress σ_{max} and the maximum of the tangent elastic modulus H_{max}. However, estimation of σ_{max} with H_{max} would be clinically difficult because the σ–ε relation in the whole range, i.e., until rupture, is necessary in order to obtain H_{max}. We also obtained a significant correlation between σ_{max} and the yielding parameter τ_σ. The parameter τ_σ was obtained from the H–σ relation by fitting Eq. 7 to the relation, and H was obtained from the σ–ε relation during pressurization. Unlike H_{max}, the parameter τ_σ can be obtained from the H–σ relation, i.e., the σ–ε relation in a relatively low pressure range. The σ–ε relation *in vivo* from diastolic to systolic pressure may give the parameter τ_σ. Calculation of wall stress requires measures of the curvature radius and thickness of the aneurysm, as well as blood pressure data *in vivo*, and calculation of strain requires deformation of the blood vessels. These parameters could be obtained noninvasively in clinical data. Thus, we might be able to estimate the failure strength of the aneurysm wall from data obtained during normal medical care. For the clinical application of this method, numerical technique will be absolutely necessary to obtain stress in the aortic wall since the shape of the diseased vessels is complicated. These techniques may enable us to estimate risks of local rupture more precisely.

Wilson *et al.*[22] reported that a decrease in the pressure strain elastic modulus of abdominal aortic aneurysms over time significantly reduced the time to rupture. The results obtained in the present study can explain their results experimentally, i.e., stiffness is well correlated with ultimate stress as shown in Fig. 8a. Their study showed that the change in stiffness of whole aneurysms correlated with their rupture risk. The present study showed that the stiffness can predict the strength of the aortic wall.

In five TAA specimens, the points of crack initiation were near the edge of the hole of the metal plate. These phenomena were not observed for PTA specimens, in which the point of crack initiation was around the center of the specimen. This might be because the curvature radius of the specimens is largest at the center area, i.e., the in-plane stress is highest at that region. The reason why the cracks began at the edge site in TAAs might be due to the existence of a stress concentration region at the edge sites. It might be easier for TAA specimens to have more stress concentration around the fixed point of the specimen because the TAA specimen is stiffer and more heterogeneous. However, since rupture at the edge sites was not found in PTA specimens, further analysis focusing on the stiffness and heterogeneity in the specimen at the microscale level will be required.

Canham *et al.*[5] reported that collagen orientation of intracranial aneurysm abruptly changed between layers. On the other hand, collagen in healthy aorta seems to orient circumferentially because SMCs orient in the direction. Therefore, the collagen direction in TAA specimens might be non-uniform, causing the diverse directions of crack propagation.

Some words of caution are in order. First, since we were not able to obtain healthy human specimens, we used porcine aorta obtained at a local slaughterhouse as a control. Although the mechanical properties of thoracic aortas of young pigs might not exactly match those of elderly people, it has been reported that there was no significant difference in the elastic modulus between the human and pig aorta.[10] Correlations between the ultimate stress and the tangent elastic modulus, and between the ultimate stress and the parameter τ_σ obtained in this study were almost similar for human and porcine aortas (Fig. 8). Taken together, we believe that the use of the porcine aorta did not cause a critical problem. Second, we calculated the mean stresses and strains of each specimen under the assumption of material homogeneity for the analysis of stiffness. On the other hand, we showed that the mechanical parameters such as local area strain were heterogeneous within a single specimen. To analyze the data precisely, the local strain obtained in this study and local stress data based on the local curvature and thickness of the specimen should be used. Third, it should be noted that a typical curvature radius of specimens on the experimental setup was ~8 mm, which was much smaller than the curvature radius of realistic geometries of aneurysms *in vivo* as shown in Table 1 (curvature radius was comparable to the half of diameter). Such difference in specimen curvature might have some effects on the mechanical properties. However, as long as the rupture properties are considered, the difference in the curvature radius had no significant effect: ultimate stress obtained in the pressure-imposed test was comparable to that obtained in a uniaxial tensile test.[13] This may indicate that the changes in curvature radius did not have marked effects on the present results.

In summary, the ultimate stress σ_{max} was correlated significantly with maximum tangent elastic modulus H_{max} and with the yielding parameter τ_σ. The maximum tangent elastic modulus H_{max} is difficult to obtain from clinical data *in vivo*, while the yielding parameter τ_σ could be obtained from clinical data. This indicates that the parameter τ_σ might be one of the candidate indices for prediction of aneurysmal rupture. We also found that TAA specimens were more heterogeneous